

AD-A184 752 THE DYNAMICS OF BUBBLE GROWTH FOR RAYLEIGH-TAYLOR

1/1

THE DYNAMICS OF BUBBLE GROWTH FOR RAYLEIGH-TAYLOR

UNSTABLE INTERFACES(U) COPENHAGEN UNIV (DENMARK)

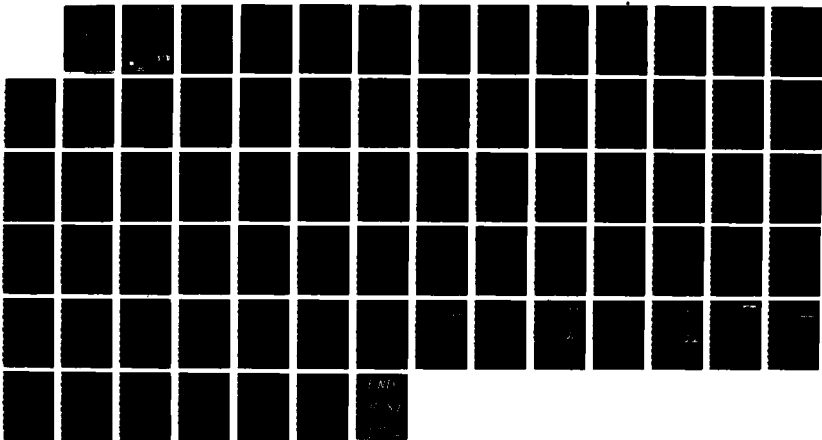
C L GARDNER ET AL MAY 87 ARO-22770 7-MA

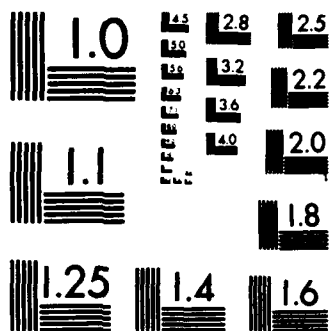
UNCLASSIFIED

DAAG29-85-K-0188

F/G 20/4

MI





MICROCOPY RESOLUTION TEST CHART
NATIONAL BUREAU OF STANDARDS-1963-A

AD-A184 752

ARJ 22770.7-M

DTIC FILE COPY

2

DOE/ER/03077-282

Courant Mathematics and
Computing Laboratory

U.S. Department of Energy

The Dynamics of Bubble Growth for Rayleigh-Taylor Unstable Interfaces

C. Gardner, J. Glimm, O. McBryan,
R. Menikoff, D. Sharp, and Q. Zhang

Research and Development Report

Supported by the Applied Mathematical Sciences
subprogram of the Office of Energy Research,
U.S. Dept. of Energy under
Contract DE-AC02-76ER03077

Mathematics and Computers

May 1987

DTIC
ELECTE
SEP 28 1987
S D E



NEW YORK UNIVERSITY

This document has been approved
for public release and sale its
distribution is unlimited.

87 9 9 243

UNCLASSIFIED

DOE/ER/03077-282

UC-32

Mathematics and Computers

THE DYNAMICS OF BUBBLE GROWTH FOR
RAYLEIGH-TAYLOR UNSTABLE INTERFACES

C. Gardner, J. Glimm, O. McBryan,
R. Menikoff, D. Sharp, and Q. Zhang

May 1987



Accession For	
NTIS GRA&I	<input checked="checked" type="checkbox"/>
DTIC TAB	<input type="checkbox"/>
Unannounced	<input type="checkbox"/>
Justification	
By _____	
Distribution/	
Availability Codes	
Dist	Avail and/or Special
A-1	

Supported by the Applied Mathematical Sciences
subprogram of the Office of Energy Research,
U. S. Department of Energy under Contract No.
DE-AC02-76ER03077

UNCLASSIFIED

DISCLAIMER

This report was prepared as an account of work sponsored by an agency of the United States Government. Neither the United States Government nor any agency thereof, nor any of their employees, makes any warranty, express or implied, or assumes any legal liability or responsibility for the accuracy, completeness, or usefulness of any information, apparatus, product, or process disclosed, or represents that its use would not infringe privately owned rights. Reference herein to any specific commercial product, process, or service by trade name, trademark, manufacturer, or otherwise, does not necessarily constitute or imply its endorsement, recommendation, or favoring by the United States Government or any agency thereof. The views and opinions of authors expressed herein do not necessarily state or reflect those of the United States Government or any agency thereof.

Printed in U.S.A.

Available from

National Technical Information Service
U.S. Department of Commerce
5285 Port Royal Road
Springfield, VA 22161

Table of Contents

	Page
Abstract	1
I. Introduction	2
A. Results, Methods and Goals	2
B. Bubble Merger and Acceleration of the Bubble Interface	3
II. A Formulation of the Statistical Model	5
III. A Qualitative Study of the Statistical Model	7
IV. A Numerical Study of the Statistical Model	9
V. Numerical Determination of the Model Parameters	16
A. The One Body Problem	16
B. The Two Body Problem	24
C. Heterogeneity	24
VI. Validation of Single Finger Computations	25
Acknowledgments	27
Appendix: The Linearized Compressible Rayleigh-Taylor Theory	27
References	33
Figure Captions	34
Figures	39

UNCLASSIFIED

MASTER COPY

FOR REPRODUCTION PURPOSES

SECURITY CLASSIFICATION OF THIS PAGE

REPORT DOCUMENTATION PAGE

1a. REPORT SECURITY CLASSIFICATION Unclassified		1b. RESTRICTIVE MARKINGS	
2a. SECURITY CLASSIFICATION AUTHORITY		3. DISTRIBUTION/AVAILABILITY OF REPORT Approved for public release; distribution unlimited.	
2b. DECLASSIFICATION/DOWNGRADING SCHEDULE		5. MONITORING ORGANIZATION REPORT NUMBER(S) ARO 22770.7-MA	
4. PERFORMING ORGANIZATION REPORT NUMBER(S)		7a. NAME OF MONITORING ORGANIZATION U. S. Army Research Office	
6a. NAME OF PERFORMING ORGANIZATION New York University	6b. OFFICE SYMBOL (If applicable)	7b. ADDRESS (City, State, and ZIP Code) P. O. Box 12211 Research Triangle Park, NC 27709-2211	
6c. ADDRESS (City, State, and ZIP Code) New York, NY 10012	9. PROCUREMENT INSTRUMENT IDENTIFICATION NUMBER DAAG29-85-K-0188		
8a. NAME OF FUNDING/SPONSORING ORGANIZATION U. S. Army Research Office	8b. OFFICE SYMBOL (If applicable)	10. SOURCE OF FUNDING NUMBERS PROGRAM ELEMENT NO. PROJECT NO. TASK NO. WORK UNIT ACCESSION NO.	
8c. ADDRESS (City, State, and ZIP Code) P. O. Box 12211 Research Triangle Park, NC 27709-2211		11. TITLE (Include Security Classification) The Dynamics of Bubble Growth for Rayleigh-Taylor Unstable Interfaces	
12. PERSONAL AUTHOR(S) C. Gardner, J. Glimm, O. McBryan, R. Menikoff, D. Sharp and Q. Zhang			
13a. TYPE OF REPORT Technical	13b. TIME COVERED FROM TO	14. DATE OF REPORT (Year, Month, Day) May 1987	15. PAGE COUNT 69
16. SUPPLEMENTARY NOTATION The view, opinions and/or findings contained in this report are those of the author(s) and should not be construed as an official Department of the Army position, policy, or decision, unless so designated by other documentation.			
17. COSATI CODES FIELD GROUP SUB-GROUP		18. SUBJECT TERMS (Continue on reverse if necessary and identify by block number)	
19. ABSTRACT (Continue on reverse if necessary and identify by block number) <p>A statistical model is analyzed for the growth of bubbles in a Rayleigh-Taylor unstable interface. The model is compared to solutions of the full Euler equations for compressible two phase flow, using numerical solutions based on the method of front tracking. The front tracking method has the distinguishing feature of being a predominantly Eulerian method in which sharp interfaces are preserved with zero numerical diffusion. Various regimes in the statistical model exhibiting qualitatively distinct behavior are explored. It appears that the parameters in the statistical model can be set from first principles on the basis of comparison with numerical solutions of the full Euler equation.</p>			
20. DISTRIBUTION/AVAILABILITY OF ABSTRACT <input type="checkbox"/> UNCLASSIFIED/UNLIMITED <input type="checkbox"/> SAME AS RPT. <input type="checkbox"/> DTIC USERS		21. ABSTRACT SECURITY CLASSIFICATION Unclassified	
22a. NAME OF RESPONSIBLE INDIVIDUAL		22b. TELEPHONE (Include Area Code)	22c. OFFICE SYMBOL

THE DYNAMICS OF BUBBLE GROWTH FOR RAYLEIGH-TAYLOR UNSTABLE INTERFACES

C. L. Gardner

Departments of Mathematics and Computer Science
Duke University
Durham, NC 27706

J. Glimm

O. McBryan^a

Courant Institute of Mathematical Sciences^b
New York University
New York, N.Y. 10012

Los Alamos National Laboratory
Los Alamos, NM 87545

R. Menikoff

D. H. Sharp

Los Alamos National Laboratory
Los Alamos, NM 87545

Q. Zhang

Courant Institute of Mathematical Sciences
New York University
New York, N.Y. 10012

ABSTRACT

A statistical model is analyzed for the growth of bubbles in a Rayleigh-Taylor unstable interface. The model is compared to solutions of the full Euler equations for compressible two phase flow, using numerical solutions based on the method of front tracking. The front tracking method has the distinguishing feature of being a predominantly Eulerian method in which sharp interfaces are preserved with zero numerical diffusion. Various regimes in the statistical model exhibiting qualitatively distinct behavior are explored. It appears that the parameters in the statistical model can be set from first principles on the basis of comparison with numerical solutions of the full Euler equation.

^{a)} Part of this work was performed during a visit at the Cornell Center for Theory and Simulation

^{b)} Permanent Address

I. INTRODUCTION

A. Results, Methods and Goals

The purpose of this paper is to formulate a program for the statistical analysis of the long time growth of bubbles formed by Rayleigh-Taylor unstable interfaces. In addition, this paper will carry out some initial stages of the program. There are two essential ingredients to this program. The first is an unpublished statistical model¹ for bubble growth and cannibalization, developed by one of the authors (D. H. S.) and J. A. Wheeler in 1961. An important prediction of this model which we further investigate and quantify is that bubble merger leads to an accelerated growth rate of the interface. The second ingredient is a front tracking hydrodynamics code, suitable for the study of unstable interfaces, developed by the authors and coworkers.²⁻⁷

There are two main new results in this paper. We have carried out a careful study up to late times of the dynamics of a single mode (bubble and spike) for a Rayleigh-Taylor interface in the compressible regime. Moreover we have identified new regimes and correlations in the interactions of ensembles of large numbers of bubbles through a study of the statistical model for bubble dynamics. These results are placed in a context, which if developed further, could allow a first principles understanding of the Rayleigh-Taylor mixing layer.

The statistical model contains two free parameters, which are the velocity of a single bubble and the relative location for merger of two adjacent bubbles. These parameters can be viewed as describing the essential features of the one and two body bubble dynamics. By a study of one and two body bubble dynamics in the full Euler equations of fluid dynamics, using the front tracking code, we can set these parameters and analyze their dependence on density ratios, compressibility, equation of state, geometry, viscosity and surface tension. In principle their dependence on spatial dimensions can similarly be determined, by use of three dimensional computations.

Once the parameters of the statistical model have been fixed, it can be studied on its own right. The most basic question is the possible existence of distinct parameter regimes or domains of initial data producing qualitatively distinct behavior (e.g. regular or quasi-uniform vs. runaway or single finger dominant modes). Any well

defined boundaries or separatrices which might exist between such domains could be thought of as defining a phase transition in the statistical behavior of an ensemble of bubbles. Within a single solution domain, the time evolution of statistical averages such as the average bubble size, height or velocity are important. Moreover the stability or insensitivity of these quantities to statistical noise in the initial conditions will also be important.

The program presented here, for the analysis of bubble dynamics, is only part of a larger question, which is a theory of the Rayleigh-Taylor mixing layer. The mixing layer can be analyzed in terms of various regions, of which the bubble regime is only one, located at the edge of the mixing layer closest to the undisturbed heavy fluid. There is a second regime, dominated by spikes or droplets at the edge of the undisturbed light fluid. A theory known as dusty gas could be appropriate for this region. It has not been determined whether additional interior regimes are needed for a full description of the mixing layer. Such a theory should describe blobs of heavy material moving at a terminal velocity and shedding vortices (Atwood ratio $A < 1$) or in free fall without vortices ($A = 1$), while the pinch off of sheets into spikes and spikes into droplets would seem to depend on surface tension. Regimes in the time evolution of the mixing layer can also be identified, such as the small amplitude (linear), the coherent individual mode, the mode competition and the chaotic regimes.⁸ Mixing theories have been advanced in a number of other contexts as well⁹⁻¹¹ See ref.¹² for a previous study of the compressible Rayleigh-Taylor problem.

B. Bubble Merger and Acceleration of the Bubble Interface

The present study goes beyond previous Rayleigh-Taylor studies in a number of respects. In doing this, we make use of the unique capabilities of the front tracking code. The detailed study of the one body bubble problem presented here for compressible Rayleigh-Taylor fingering seems to be the first attempt to set the parameters of the Sharp-Wheeler model from a first principles calculation. Youngs has argued⁸ that deeply nonlinear multi-mode computations of the chaotic regime are necessary to understand the Rayleigh-Taylor chaotic mixing regime. Since such computations are at best only marginally possible and of uncertain validity in their prediction of statistical mixing phenomena, it is significant that some statistical information

may be extracted from the study of the one and two bubble problems. A test of these predictions would be to compare them to direct simulation of the deeply nonlinear chaotic regime, using front tracking and other methods. The computational analysis of the Sharp-Wheeler model is also new. The identification of a transient exponentially growing runaway mode in the bubble merger process and the importance of nearest neighbor correlations in limiting bubble amalgamation appears to be new. The constant acceleration rate^{1,8,13} of the bubble interface has been confirmed in the examples of initial data considered, but the rate has been found to depend on initial conditions, and seems not be a universal constant at least for the time periods explored in this paper. Youngs' argument⁸ in favor of universality was based on a scaling argument and on an absence of extra length scales in the problem. Our example of non-universal acceleration rates depends on introducing an extra length scale. This was introduced by slightly varying the bubble radii, so that the deviation in radius was much smaller than the mean radius. Because of the presence of a length scale in the initial data, we do not contradict the scaling argument of Youngs, but we do suggest that his hypothesis of the absence of extra length scales may be valid only for a restricted class of Cauchy data or for extremely late times. Experimental results on carefully prepared interfaces reveal a universal behavior, with the bubble interface height $h = h(t)$ satisfying the relation $h = \alpha g A t^2$ and $\alpha \approx .06$ (two dimension) or $\alpha \approx .07$ (three dimension)¹⁵, where A is the Atwood ratio, $A = \frac{\rho_b - \rho_a}{\rho_b + \rho_a}$. Here ρ_a is the density of the gas above the interface, and ρ_b is the density of the gas below the interface.

Other mechanisms leading to a constant acceleration, $\alpha g A t^2$, of the bubble interface are possible. For an initial time period, the bubbles accelerate (are in free gravitational rise). For the strongly compressible case considered here, the bubbles attain velocities up to Mach 2 relative to the sound speed of the heavy gas. Comparing our values for free rise renormalized gravity ($\approx .5Ag$) for bubbles, we get a position $h \approx .25Ag t^2$ by this mechanism, which is approximately four times the position predicted by the merger mechanism, according to Read's data. Free rise describes an earlier time period than the merger process, and compressibility plays a major role in setting the duration of this earlier regime.

A second possible mechanism for constant acceleration is that random initial data may contain a mixture of large and small wavelengths. The small wavelengths grow more rapidly at first but then saturate and eventually the initially slower large wavelengths become faster and win out. Thus large structures may be latent in the initial data, and emerge gradually over time, leading to an acceleration of the bubble interface. Neither of these alternate mechanisms appear to be important in Read's data.

Portions of our results have been announced previously.¹⁵⁻¹⁷ (See ref.¹⁸ for a further discussion of this problem).

II. A FORMULATION OF THE STATISTICAL MODEL

The main idea in the statistical model is to introduce a very reduced set of parameters ("idealized interfaces") and a simplified interface dynamics, which captures the essential features of the full flow in the mixing layer. For comparison purposes, we also need a map from arbitrary to idealized interfaces. It is then hoped that the stable statistical properties (average bubble size, etc.) of the model will correspond to stable statistics of the full flow and that after adjustment of model parameters, the dynamics of such stable statistical properties will approximate the true dynamics of such stable properties of the full flow.

The first approximation we make in going from the full flow to the model is to assume that the interface position at time t is a single valued function $z = z(x, y, t)$ of the point x, y . We do not assume x, y, z to be a rectangular set of coordinates, and so various curvilinear geometries are included in this analysis. Let us suppose that the heavy fluid is located in the region $z < z(x, y, t)$ below the interface and that the accelerating force is in the direction of the positive z axis.

Since a Rayleigh-Taylor unstable interface at late time will be far from single valued and since we are developing here a theory of the bubble region only, within the mixing layer, we regard $z(x, y, t)$ as representing a "bubble envelope" equivalent to the true interface, defined precisely by the imposition of mass conservation along each line $x = \text{const.}$, $y = \text{const.}$ Thus if the entire multivalued interface lies below some reference height z_0 , we define

$$z(x, y, t) = z_0 - L(x, y, t, z_0)$$

where L is the length of the portion of the line $x = \text{const.}$, $y = \text{const.}$ located in the light fluid above z_0 .

Next we fix a set of bubble boundaries, which in mathematical language is a tiling of the surface $z = 0$ by polyhedra. In two space dimensions, the bubbles thus define a decomposition of the x axis into non-overlapping intervals. Even in this simplest case, we do not propose a general algorithm for the placement of bubble boundaries, but we will return to this question as part of a detailed analysis of when or whether merger occurs in the two body bubble interaction problem.

Finally the model assumes that the fluid is piecewise constant, and constant within each bubble. Given a bubble decomposition (polyhedral tiling) of a general single valued interface $z = z(x, y, t)$, the principle of mass conservation again defines a corresponding interface within the model, i. e. piecewise constant on each bubble.

The kinematics of the model is now determined; we must specify its dynamics. There are two processes allowed in the dynamics of the model: vertical motion and merger. We assume that each bubble moves vertically with a velocity \dot{z} which is independent of the bubble height and the other bubbles. Thus \dot{z} is a function of the bubble shape alone. We note that for a circular bubble of vacuum, with radius r , rising in an incompressible fluid in three space dimensions, Taylor's formula gives

$$-\dot{z} = .48 (gr)^{\frac{1}{2}}. \quad (1)$$

In two dimensions, $\dot{z} = \dot{z}(r)$, is thus assumed to be a function of the bubble radius alone. As a further approximation in three dimensions, we define an effective radius $r = (\frac{\text{Area}}{2\pi})^{\frac{1}{2}}$ and postulate that $\dot{z} = \dot{z}(r)$ in this case also. In effect, this means that the bubbles do not depart too greatly from a circular cross section.

The remaining aspect of the model bubble dynamics is merger. It is postulated that adjacent bubbles merge when one is sufficiently far ahead of the other. After merger, there is a single bubble, with cross section equal to the union of the cross sections of its two constituents and a height z determined by conservation of mass within this cross section. If the heights and radii of the two bubbles before merger are z_i and r_i , $i = 1, 2$, then we formulate the merger criterion as

$$z_2 - z_1 \leq -m(r_1) \quad (2)$$

where $r_1 \leq r_2$ and $m(r)$ is an unknown function of r .

Thus the statistical model is defined by two unknown functions, $z(r)$ and $m(r)$, which express the essential features of the one and two body bubble problems respectively. These functions must then be set either by some external theory or experiments or by a numerical study of these one and two body problems in the full Euler equations.

One aspect of this model is that after merger the new bubble may also satisfy the merger criterion with an adjacent bubble thus giving rise to a cascade of mergers at a single instant of time. For example, a cascade occurs if the next nearest neighbor of a large bubble is smaller than its nearest neighbor and the height of the next nearest neighbor is less than the height of the nearest neighbor. Thus the merger process in this model for some distributions of bubbles consists of more than two body interactions.

III. A QUALITATIVE STUDY OF THE STATISTICAL MODEL

We assume a probabilistic distribution of initial data in the form of bubble heights and widths. It should be noted that the model of Section 2 is actually deterministic, and becomes a statistical model at this point alone. For simplicity we now consider bubbles in two dimensions. From a fundamental point of view, we imagine a translation invariant ensemble of random bubble interfaces, constrained to be defined by single valued piecewise constant functions $z = z(x)$. This ensemble is fully described by a set of n -point functions or correlation functions, i.e. conditional probability distributions for a sequence of n adjacent bubble widths and heights. The model dynamics is equivalent to an infinite system of coupled partial differential equations for these n point functions. This system does not close, in the sense that the equations for the j point functions, $1 \leq j \leq n$, depend on the $n + 1$ point function. We invoke the simplest closure hypothesis, assuming that the statistical properties of points are independent, or equivalently that the truncated two point function is zero. In the next section it will be shown that this closure hypothesis excludes an important range of phenomena. Let $\eta(w, z, t)$ be a density function for the distribution of bubble widths w and heights z at time t . The closure hypothesis leads to a nonlinear set of coupled partial differential equations for η . Namely

$$\frac{\partial}{\partial t} \eta(w, z, t) + \dot{z} \frac{\partial}{\partial z} \eta(w, z, t) = B - D.$$

Here B and D are the birth and death terms respectively, resulting from bubble merger, while the left hand side expresses the noninteracting growth of a single bubble. Specifically

$$B(w, z, t) = \int_{\mathcal{D}_B} \eta(w', z', t) \eta(w'', z'', t) |\dot{z}(w') - \dot{z}(w'')| dw',$$

$$D(w, z, t) = 2\eta(w, z, t) \int_{\mathcal{D}_D} \eta(w', z', t) |\dot{z}(w') - \dot{z}(w)| dw',$$

where \mathcal{D}_B and \mathcal{D}_D specify domains of integration, defined as follows:

$$\mathcal{D}_B = D_{width} \cap D_{mass} \cap D_{merge}$$

$$\mathcal{D}_D = \{w', z': 0 \leq w \leq w' \text{ and } z' - z = m(w)\}$$

$$\cup \{w', z': 0 \leq w' \leq w \text{ and } z - z' = m(w')\}.$$

Here D_{width} , D_{mass} and D_{merge} denote the conservation of width and mass and the merger height constraints respectively.

$$D_{width} = \{w', z', w'', z'': w' + w'' = w \text{ and } w', w'' \geq 0\},$$

$$D_{mass} = \{w', z', w'', z'': w' z' + w'' z'' = w z\},$$

$$D_{merge} = \{w', z', w'', z'': w'' \leq w' \text{ and } z' - z'' = m(w'')\}$$

$$\cup \{w', z', w'', z'': w' \leq w'' \text{ and } z'' - z' = m(w')\}$$

In order to continue the analysis we assume a distribution in the heights z and bubble widths w , which are characterized by time dependent parameters, such as their means and covariances. Differential equations can then be derived for these parameters, which however will not close, in the sense that time derivatives of the distribution will not in general lie in the same finite dimensional subspace characterized by these parameters. Again we impose a closure hypothesis, which corresponds to a projection of the dynamics onto a fixed finite dimensional subspace. We do not pursue this point of view further in the present paper.

IV. A NUMERICAL STUDY OF THE STATISTICAL MODEL

There are two constants, c_1 and c_2 , which characterize the statistical model, namely

$$-\dot{z}(r) = c_1(gr)^{\frac{1}{2}} \quad (3)$$

and, with the further simplifying assumption that $m(r)$ is linear,

$$m(r) = c_2 r, \quad (4)$$

cf. (1) and (2). To begin with, we consider the model in the x, z plane. Then the mean bubble size fixes the x units, c_2 fixes the relation of the z units to the x units, and g fixes the relation of the z unit to the time units. $\frac{c_1^2}{c_2}$ is a dimensionless free parameter of the model. Moreover, the mean height fixes the origin of the z units. Thus the only essential parameters are the dimensionless variances $\frac{\text{var}(r)}{r}$, and $\frac{\text{var}(h)}{c_2 \langle r \rangle}$ and higher moments characterizing the initial data of the bubble size and height distributions. Here $\text{var}(x) = \frac{\langle x^2 \rangle - \langle x \rangle^2}{\langle x \rangle}$. Next we consider the model in an infinite strip, $x_0 \leq x \leq x_1$. The ratio of mean bubble size to interval width, $x_1 - x_0$ is a dimensionless measure of the distance of the data from the final equilibrium state of a single bubble. If the strip is finite, $z_0 \leq z \leq z_1$, then another dimensionless parameter is introduced which measures the time at which the interface exits as a fraction of the time to achieve the single bubble equilibrium state.

The essential phenomena which this model aims to capture is the increase in average bubble size, and the consequent increase in average bubble velocity, resulting from the process of amalgamation. In order to study the amalgamation quantitatively, we introduce a growth rate

$$\lambda = \frac{d \ln r}{dt},$$

where r is a typical bubble radius. From (3), we see that

$$\lambda = \frac{\dot{r}}{r} = \frac{2}{v} \frac{dv}{dt},$$

where $v = \dot{z}$ is a typical bubble velocity.

The mean radius of the bubbles increases in time because the model is based on bubble mergers and has no mechanism by which a bubble can split into smaller bubbles. As a result, the possible patterns of growth of the ensemble of bubbles can be conveniently discussed with reference to two extreme cases; uniform growth and runaway growth. Uniform growth is the analog of a steady state and is characterized by a translation of the ensemble distribution in $\ln r$ with time. Runaway growth is the approach to a fixed point consisting of one large bubble. Each of these cases may be characterized by the dynamics of the support of the ensemble of bubble radii in $\ln r$ space. In the case of uniform growth, the support of the bubble distribution in $\ln r$ space has a bounded length, which is $O(1)$ in time. At the other extreme is the case of runaway growth, in which the support of the bubble distribution shows marked increase in length as a function of time because the radius of the large dominant bubble grows at a greater rate than the mean radius. To make these ideas quantitative, we define the length of the support to be $\ln r_{\max} - \ln r$ where r_{\max} is the radius of the largest bubble in the ensemble and r is again a typical bubble radius.

We also distinguish two time periods in the evolution of the bubble ensemble. We suppose initially that the bubbles are generated by a random process, and thus that the distribution of a given bubble (i.e. its radius and height, considered as random variables) is independent of its neighbor. In other words adjacent bubbles are uncorrelated, and so the truncated two point correlation function is initially zero. Under this hypothesis, we give an approximate analysis which shows that the regime of uniform growth is unstable and that runaway growth occurs. We also present numerical evidence which shows this trend very clearly.

However, correlations between the sizes of neighboring bubbles do arise dynamically even if they are missing initially. In fact a large bubble will grow rapidly in radius by the merger process when placed in a field of much smaller bubbles, but rather slowly when placed in a field of only slightly smaller bubbles. Thus after an initial period, large bubbles are more likely to have large neighbors: they expand until this occurs to limit or retard their growth. In this case the runaway behavior is self-limiting and a regime of uniform growth appears to be stable. We present numerical evidence for the stabilization of bubble runaway through the mechanism of dynamically generated nearest neighbor correlations.

First we examine an initial period of uncorrelated nearest neighbor distributions. To better understand the behavior of the two regimes of uniform and runaway growth, we derive an approximate formula for the growth rates λ and $\lambda_{\max} = \frac{\dot{r}_{\max}}{r_{\max}}$.

Consider a local region of space in which a single large bubble is growing in a uniform background field of small bubbles of radius r . We also assume a small distribution of heights for the background bubbles. Because the velocity increases with radius, the large bubble will eventually get ahead of the background bubbles. The height of the large bubble is then fixed at a height $c_2 r$ above the height of the small bubbles. This constraint, combined with the conservation of mass in the merger process, forces the rapid growth of the large bubble to be primarily in the lateral direction. The rate at which bubble mass is created in a large bubble is $2r_{\max} c_1 \sqrt{gr_{\max}}$. Normalizing for the effect of motion of the small bubbles gives a corrected mass rate of $2r_{\max} c_1 [(gr_{\max})^{\frac{1}{2}} - (gr)^{\frac{1}{2}}]$. Thus the time rate of change $2\dot{r}_{\max}$ of the diameter is obtained by dividing the latter expression by the difference in height between the small and large bubbles, $c_2 r$. Thus

$$\lambda_{\max} = \frac{\dot{r}_{\max}}{r_{\max}} = \frac{c_1}{c_2} r^{-1} [(gr_{\max})^{\frac{1}{2}} - (gr)^{\frac{1}{2}}].$$

When $r_{\max} \gg r$, equation (3) implies the approximate formula

$$\lambda_{\max} = \frac{c_1^2}{c_2} \frac{r_{\max}}{r} \frac{g}{v_{\max}}.$$

We note that the growth rate λ_{\max} goes to ∞ with the aspect ratio, if either r_{\max} or r is held fixed. Hence the name "runaway mode" to discuss the case in which this occurs. It is convenient to consider $\ln r$ rather than r as the basic variable in terms of which the radial distribution is specified. Thus we define $(\delta \ln r)_{\max}$ through the formula

$$r_{\max} = \exp(\ln r + (\delta \ln r)_{\max})$$

and then

$$\lambda_{\max} = \frac{c_1}{c_2} \left(\frac{g}{r} \right)^{\frac{1}{2}} \left[\exp\left(\frac{(\delta \ln r)_{\max}}{2} \right) - 1 \right].$$

To complete our semi-quantitative analysis of the stability of the bubble ensemble, we derive a formula for the growth rate λ . Consider two adjacent bubbles having radii r_+ and r_- respectively. For simplicity, we suppose that initially the bubbles have equal heights. We determine the time to merge, t_m , for this pair, and postulate that this time is the doubling time of the mean radius r . On this basis we determine the growth rate λ in the following equations

$$2r = e^{\lambda t_m} r$$

or

$$\lambda = \frac{\ln 2}{t_m}.$$

Moreover, t_m is determined from the equations of motion of the model, (3)-(4), to be

$$t_m = \frac{c_2}{c_1} \left[(gr_+)^{\frac{1}{2}} - (gr_-)^{\frac{1}{2}} \right]^{-1} r_-.$$

We choose r_{\pm} as

$$r_{\pm} = \exp(\ln r \pm \frac{\delta \ln r}{2}).$$

Then

$$\lambda = \frac{c_1}{c_2} \ln 2 \left(r_+^{\frac{1}{2}} - r_-^{\frac{1}{2}} \right) r^{-1}$$

and taking ratios,

$$\frac{\lambda_{\max}}{\lambda} = \frac{1}{\ln 2} \frac{r_-}{r} \frac{\left(\frac{r_{\max}}{r} \right)^{\frac{1}{2}} - 1}{\left(\frac{r_+}{r} \right)^{\frac{1}{2}} - \left(\frac{r_-}{r} \right)^{\frac{1}{2}}}$$

or

$$\frac{\lambda_{\max}}{\lambda} = \frac{1}{\ln 2} \exp\left(-\frac{\delta \ln r}{4}\right) \frac{\exp\left(\frac{(\delta \ln r)_{\max}}{2}\right) - 1}{\exp\left(\frac{\delta \ln r}{2}\right) - 1}. \quad (5)$$

From these formulas, we see that two essential parameters which describe the input statistics have a critical bearing on the stability (uniform or runaway growth) of the bubble merger process. These parameters are the variance and the maximum

deviation, $\delta \ln r$ and $(\delta \ln r)_{\max}$ of the $\ln r$ distribution. Similarly the variance and maximum deviation of the height / radius distribution are essential parameters. In addition to acting as above as a cause of instability, the height variation can, at least initially, contribute to stability. The mechanism is as follows. If small bubbles are placed ahead of and adjacent to large ones, they will retard temporarily the merger process of those larger bubbles.

Analysis of (5) shows stability ($\frac{\lambda_{\max}}{\lambda} < 1$) or uniform growth for

$$\frac{(\delta \ln r)_{\max}}{\delta \ln r} \sim 1. \quad (6)$$

However (6) cannot be achieved, except for the identically uniform distribution of bubbles in which each has the same radius and height. The formulas (5)-(6) are intended to be interpreted qualitatively rather than literally and thus we conclude that control of r_{\max} relative to r will be important in reducing the growth rate of the instability, and in delaying the onset of the runaway mode.

If the initial distribution of $\ln r$ or h has unbounded support (in the large r or h directions) then outlying large bubbles will necessarily occur and the infinite volume limit is necessarily unstable with an unbounded growth rate. In particular it would appear that the runaway period would not be self limiting and that the subsequent period of uniform growth would not occur. Our computations have not been sufficiently extensive to determine whether uniform growth will always occur for the case of an initial distribution with bounded support.

Next we discuss the relation between the infinite volume limit and a consideration of the model in a bounded strip $x_0 \leq x \leq x_1$. The effect of the finite volume is in general terms to convert absolute statements into probabilities, so that for example it would seem that for a finite volume and an initial distribution with unbounded support, a finite (non-zero) probability exists that the self-limiting uniform growth region will not occur.

We illustrate these ideas by the analysis of a series of computations. Numerically we observe a tendency for the runaway mode to be self-limiting. Large bubbles expand until they acquire large neighbors, after which uniform growth occurs. The details of this phenomena depend sensitively on the large bubble tail of the distribution, and so we do not yet have an accurate predictive capability for this region.

We analyze two computational solutions of the bubble model, labeled H (homogeneous) and L (with a length scale), in some detail. The initial distribution of heights h and radii r was chosen to be uniform over the interval

$$h \in [h_0 - \delta h, h_0 + \delta h], \quad r \in [r_0 - \delta r, r_0 + \delta r] .$$

Care was taken in generating the initial random interface to ensure that there were no sequential correlations among the bubbles. The units for both runs were chosen such that the initial average radius was $\langle r \rangle = 1$, $c_2 = 1$, and the initial mass weighted average velocity was $\langle \dot{z} \rangle = 1$. The initial average height was chosen to be $\langle h \rangle = 0$. Both runs had noisy height variation $\delta h/r_0 = 1$. Run H had noisy radial variation $\delta r/r_0 = 1$, while run L had small radial variation $\delta r/r_0 = 0.1$. To minimize statistical fluctuations the computations were started with about 10,000 bubbles.

The run H shows an initial runaway region followed by uniform growth, as described above. Run L shows two new features in addition to these general trends. Because of the small initial variation in the bubble radius, the bubble radius distribution has a "resonance" behavior, or a multimodal nature, clustered about the values nr_0 , for the bubbles formed from the merger of n initial bubbles. The second prominent feature of this run is slow start and the extended duration of the initial runaway period, and the delayed onset of the self-limiting uniform growth behavior.

In Fig. 4.1H and Fig. 4.1L, we show the location in x, t space of a sampling of new bubbles as they are created by the merger of two or more neighboring bubbles. Initially the mergers are randomly distributed. As time progresses the width of the bubbles increases. The radial distribution of bubbles in $\ln r$ space changes with time. A sequence of plots at successive time steps is shown in Fig. 4.2. At first the support of the distribution grows and then the shape of the distribution becomes smeared out.

Many aspects of the merger process can be understood from time histories of appropriate quantities. Fig. 4.3 is a plot of the log of the number of bubbles vs. time. After an initial period the number of bubbles decreases exponentially. The initial period is relatively large when there is a small variation in the radius and hence the velocities of the bubbles. The mass weighted average velocity vs. time is shown in Fig. 4.4. After an initial period of slow increase the velocity accelerates almost uniformly. This is an important consequence of the merger process. Mergers

cause the mean bubble radius to grow which results in larger velocities. Similar predictions of uniform acceleration have been stated previously.^{1,8,14} With the simple model used here we are able to study the statistics of a large number of bubbles. We find the magnitude of the acceleration depends sensitively on the bubble distribution. In Fig. 4.5 the log of the minimum, mean, and maximum bubble radius vs. time is plotted. This shows the growth of the bounds on the support of the radial distribution function. Of particular interest for the analysis of runaway growth is $\ln(r_{\max}/r_{\text{mean}})$ vs. time shown in Fig. 4.6. We see that the support grows rapidly indicating a runaway growth but then saturates resulting in a more uniform growth. In Fig. 4.7 we plot the minimum, mean, and maximum height vs time. We call attention to the fact that the maximum height is the quantity which would be relevant to the break up of a shell for example in the laser fusion problem, and that the maximum behaves qualitatively differently from the mean. Furthermore, this behavior depends on the initial bubble distribution. The spread in height in units of the mean radius is very much larger due to the runaway growth when the initial variation in radius of the bubbles is small than for an initial noisy variation in the bubble radius. The saturation in the growth of the support of the bubble distribution and the transition to a uniform growth is due to correlations which evolve dynamically. In Fig. 4.8 we plot the radius-height cross correlation, or in other words the correlation between the radius and the height of a single bubble. The large correlation is as expected and displays the fact that large bubbles move faster and get ahead of small bubbles. In Fig. 4.9 the nearest neighbor correlation in the radius and height is shown,

$$c_r = \frac{\frac{1}{N-1} \sum (r_i - \langle r \rangle)(r_{i+1} - \langle r \rangle)}{\frac{1}{N} \sum (r_i - \langle r \rangle)^2}$$

$$c_h = \frac{\frac{1}{N-1} \sum (h_i - \langle h \rangle)(h_{i+1} - \langle h \rangle)}{\frac{1}{N} \sum (h_i - \langle h \rangle)^2}$$

This indicates that bubbles grow rapidly until the adjacent bubble is larger than the mean in radius or higher than the mean in height. Thus the runaway growth is a local phenomenon that depends on a single large bubble in an approximately uniform background. For a large region this local growth pattern may occur at many widely separated places which eventually interact. Another way of seeing these correlations

which limit the runaway growth is to consider the bubbles adjacent to the largest bubbles. We use as the criterion for selecting the large bubbles,

$$\ln r > 0.2 \ln(r_{\text{mean}}) + 0.8 \ln(r_{\text{max}}) .$$

In Fig. 4.10 we plot the average bubble radius adjacent to the large bubbles in units of the mean radius and the average height of adjacent bubbles below large bubbles in units of the merge height for bubbles of mean radius. Again this plot indicates that large bubbles run into adjacent bubbles with larger than mean radius and above mean height. These runs imply that the dynamic correlations have an important effect on the merger process and that a simple qualitative model as outlined in Section III would require a non-trivial closure hypothesis to capture this phenomena.

In summary, the initial period of runaway behavior is characterized by a small but exponentially increasing bubble acceleration and a relative absence of nearest neighbor correlations. The transition to uniform growth is caused by the dynamic development of nearest neighbor correlations and is characterized by a relatively constant but large acceleration.

V. NUMERICAL DETERMINATION OF THE MODEL PARAMETERS

A. The One Body Problem

We identify three regimes for the time development of the rising bubble and for the falling spike, in the case of motion in an infinite strip, so that boundary effects can be neglected. The initial time for the spike and bubble motion is set by the initial amplitude of a sinusoidal surface. The perturbation of the initially flat interface is small, and the time evolution of the surface can be described by the linearized Euler equations. (See the Appendix.)

The isothermal equilibrium situation consists of a flat interface with exponentially stratified atmospheres above and below the interface. We consider perturbations of the unstable equilibrium in which the heavy fluid lies below the light fluid and gravity is directed upwards.

The compressible Rayleigh-Taylor problem depends on three dimensionless parameters: the density ratio $D = \frac{\rho_b}{\rho_a}$, where ρ_b is the density of the heavy gas just

below the interface and ρ_a is the density of the light gas just above the interface, the polytropic gas constant γ (here we set $\gamma_a = \gamma_b$) or other information to set the equation of state for the heavy and light fluids, and a parameter M defining the ratio of a gravitational time scale to a sound speed time scale. (M defines a dimensionless compressibility¹⁹.) We take $M^2 = \frac{g\lambda}{c_b^2}$, where λ is the wavelength of the interface perturbation and c_b is the sound speed in the unperturbed heavy fluid. In place of the density ratio D , the Atwood ratio $A = \frac{\rho_b - \rho_a}{\rho_b + \rho_a}$ may be used as a dimensionless parameter. Observe that the mass of the heavy fluid per unit cross section is finite, even though the strip it is located in is semi-infinite, due to the exponential stratification of the fluid densities. In fact this mass density is

$$\Omega = \rho_b \int_0^{\infty} \exp(-\beta y) dy ,$$

where $\beta = \frac{\gamma g}{c_b^2}$.

The initial growth at small time of both the spike and bubble is exponential. The formulation of the linear stability theory, which governs the small time behavior, was given by Bernstein and Book¹⁸ for the infinite strip. These results are given in the Appendix, and are extended to apply to a finite strip with reflecting boundary conditions at top and bottom. They are also extended to apply to a general equation of state. The dependence of the dimensionless exponential growth rate constant $\frac{c_b \sigma}{g}$ on the dimensionless parameters A and M is shown in Fig. 5.1 for $\gamma = 1.4$. In Fig. 5.1, the dimensionless growth rate contours are equally spaced, with the difference between two adjacent contours being .793. A larger value of M^2 or A gives rise to a larger dimensionless growth rate, since gravity increases with M^2 and renormalized gravity increases with A . At intermediate times, the spike enters a period of free fall. The bubble may have an intermediate period of free rise, and if it does so it is or may be Rayleigh-Taylor unstable and is therefore potentially unstable to splitting through the development of a spike at its center. At late times both the bubble and the spike approach an asymptotic constant velocity due to the form drag and the finite total mass supported above the bubble and spike. Although not present in the model equations discussed here, an experimentally more realistic late time behavior for the

spike would be a breakup into droplets which then also achieve a terminal velocity due to form drag. The regimes of free fall and of the approach to an asymptotic velocity for the spike can be modeled by a particle falling under the influence of gravity g with a drag coefficient b and limiting velocity v_{term} . The model problem

$$\dot{v} = -b(v - v_{\text{term}}) \quad (7)$$

has the first integral

$$v = v_{\text{term}} + (v_0 - v_{\text{term}}) \exp(-b(t - t_0)) \quad (8)$$

where b is the drag coefficient, v_0 is the velocity at time t_0 and v_{term} is the terminal spike velocity. Actually, equation (7) is the expansion of the dynamic equation in a neighborhood of the terminal velocity keeping only the leading term (the term linear in the velocity). Therefore equation (8) should be valid only in the terminal velocity region. To understand the behavior of the velocity over a larger domain (including the linear and free fall regions), the contribution from the higher order terms should also be included. To the third order in velocity, the dynamic equation can be written as

$$\dot{v} = a_1 v + a_2 v^2 + a_3 v^3. \quad (9)$$

One can see by inspection that equation (9) has qualitatively the desired form. Obviously, it has a critical point $v = 0$. By suitable choices of a_1 , a_2 and a_3 , it will have another critical point $|v| = |v_{\text{term}}| > 0$. In general, a third order algebraic equation should have three solutions. But, as we will see, one of the solutions is not physical. The critical velocity $v = 0$ corresponds to the velocity for a perturbation with infinitesimal initial amplitude at the interface. The system will leave this critical point exponentially and it approaches the $v = v_{\text{term}}$ critical point exponentially also. We now develop these facts systematically, and also determine how the terminal velocity, renormalized gravity in the free fall region and drag coefficient are related to the coefficients of equation (9).

In the earlier stage of the development, one may neglect the terms proportional to v^2 and v^3 in equation (9) due to the small amplitude of the velocity. Then equation (9) can be approximated as

$$\dot{v} \approx a_1 v. \quad (10)$$

This equation has the solution

$$v = v_0 \exp(a_1(t - t_0)). \quad (11)$$

We conclude $a_1 = \sigma$, by comparison to the results from the linear theory. (See the Appendix.) By a dimensional argument, a_2 must have the form $a_2 = -2\kappa \frac{\sigma^2}{g}$ and $a_3 = -\xi \frac{\sigma^3}{g^2}$, where κ and ξ are dimensionless constants and g is (the unrenormalized) gravity.

The concavity of the curve representing velocity versus time is determined by the derivative of equation (9), i.e.,

$$\frac{d^2v}{dt^2} = (\sigma - 4\kappa \frac{\sigma^2}{g}v - 3\xi \frac{\sigma^3}{g^2}v^2)v. \quad (12)$$

Then the curve at velocity v is concave up or down, depending on whether the derivative of the acceleration is positive or negative. At the inflection point the derivative of the acceleration vanishes. If we define a velocity v_f , determined by the equation

$$\sigma - 4\kappa \frac{\sigma^2}{g}v_f - 3\xi \frac{\sigma^3}{g^2}v_f^2 = 0, \quad (13)$$

then the linear theory region corresponds to the range where $v \ll v_f$, the terminal velocity region corresponds to the range where $v \gg v_f$, and the free fall region corresponds to the range where $v \approx v_f$.

The terminal velocity v_{term} is determined by setting the acceleration in equation (9) to zero, i.e.

$$\sigma v - 2\kappa \frac{\sigma^2}{g}v^2 - \xi \frac{\sigma^3}{g^2}v^3 = 0. \quad (14)$$

Obviously, $v = 0$ is not a solution for the terminal velocity. The other two possible solutions are

$$v^- = \frac{-g}{\sigma\xi}[\kappa + (\kappa^2 + \xi)^{\frac{1}{2}}] \quad (15)$$

and

$$v^+ = \frac{-g}{\sigma\xi}[\kappa - (\kappa^2 + \xi)^{\frac{1}{2}}]. \quad (16)$$

Physically, the system starts with a perturbation at the interface. The initial velocities of the spike and bubble are determined by the linear theory. The terminal velocity must have the same sign as the initial velocity. If both solutions v^\pm satisfy this sign condition, then the solution with the smaller magnitude is the terminal velocity, since the system starts at the critical point $v = 0$ and will meet the smaller amplitude solution first. Let us consider the spike first. We choose $0 < g$. For $0 < \xi$, only v^+ has the same sign as the initial spike velocity ($0 < v^+$). For $\xi < 0$ and $\kappa < 0$, both v^+ and v^- are negative and neither satisfies the sign condition. For $\xi < 0$ and $0 < \kappa$, both v^+ and v^- satisfy the sign requirement, but v^+ has the smaller amplitude. Therefore v^+ , if it is positive, is the only physical solution for the terminal velocity of the spike, while v^- is always an unphysical solution. Similarly, v^- , if it is negative, is the only physical solution for the terminal velocity of the bubble and v^+ is an unphysical solution. Furthermore, for sufficiently negative values of ξ ($\xi < -\kappa^2$), both v^+ and v^- become complex quantities. In this case the terminal region does not exist for the model system (9) in that parameter range. For the same reason equation (13) also has at most one physical solution. For the spike

$$v_f = \frac{-g}{3\sigma\xi} [2\kappa - (4\kappa^2 + 3\xi)^{\frac{1}{2}}], \quad (17)$$

and for the bubble

$$v_f = \frac{-g}{3\sigma\xi} [2\kappa + (4\kappa^2 + 3\xi)^{\frac{1}{2}}]. \quad (18)$$

Moreover renormalized gravity in the free fall region is given by

$$g_R = \left| \sigma v_f - 2\kappa \frac{\sigma^2}{g} v_f^2 - \xi \frac{\sigma^3}{g^2} v_f^3 \right|. \quad (19)$$

We rewrite equation (9) in terms of the terminal velocity. Then the coefficient of the linear term is the drag coefficient, i.e.

$$\frac{dv}{dt} \approx -b(v - v_{\text{term}}) + O[(v - v_{\text{term}})^2]$$

where

$$\begin{aligned} b &= -(\sigma - 4\kappa \frac{\sigma^2}{g} v_{\text{term}} - 3\xi \frac{\sigma^3}{g^2} v_{\text{term}}^2) \\ &= 2\sigma \left\{ 1 + \frac{\kappa}{\xi} [\kappa \pm (\kappa^2 + \xi)^{\frac{1}{2}}] \right\}. \end{aligned} \quad (20)$$

Here the plus sign is for the bubble and the minus sign is for the spike.

The solution for equation (9) is

$$t - t_0 = \frac{-g^2}{\xi \sigma^3} \left[\frac{1}{v^+ v^-} \ln\left(\frac{|v_t|}{|v_0|}\right) + \frac{1}{v^+(v^+ - v^-)} \ln\left(\frac{|v_t - v^+|}{|v_0 - v^+|}\right) + \frac{1}{v^-(v^- - v^+)} \ln\left(\frac{|v_t - v^-|}{|v_0 - v^-|}\right) \right]. \quad (21)$$

where $v_t = v(t)$ is the velocity at time t , and v^+ and v^- are given by equations (15) and (16). This is the formula we use to fit the velocities of the bubble and spike simultaneously over all three different (linear, free fall and terminal) regions. There are two free parameters in (21) which can be adjusted to fit the computed curve of spike velocity vs. time, as shown in Fig. 5.2. The computed spike and bubble velocities were smoothed by averaging before plotting to eliminate oscillations of a numerical nature in the data.

In Fig. 5.3, we illustrate the spike dynamics in three (linear, free fall and terminal) regions. Renormalized gravity corresponds to the maximum acceleration over the whole time domain. This is a consequence of our discussion concerning the concavity of the velocity curve. When the system goes from the linear region to free fall, the deviation of the linear theory from the results for the full Euler equation becomes substantial. Likewise before the system enters the terminal region, the results from the asymptotic behavior (Eq. (7)) give a more rapid deceleration than the true value.

In Fig. 5.4, we present the dependence of the gravity renormalization factor g_R/g defined by equation (19) on the density ratio D . The data (from reference 20) for two dimension incompressible ($M^2 = 0$), one component ($A = 1$) flow are also shown. The incompressible data may be affected by the large initial amplitude (0.5) used in the cited computation. Our computational data show that the renormalization factor depends linearly on the Atwood ratio A and $g_R \approx .5Ag$ for the bubble, while $g_R \approx Ag$ for the spike.

At equilibrium, the right side of equation (15) vanishes, and in this case we have an expression for the drag $d = L_{b+s}\Omega g$ where L_{b+s} is the combined width of the bubble and spike. Ω is the mass density given at the beginning of this section. It is convenient to introduce the dimensionless drag coefficient of the spike following

reference ²⁰

$$C_D = 2 \frac{d}{\rho_a v_{\text{term}}^2 L_s}, \quad (22)$$

where L_s is the width of the spike tip. Substitution of the expression for d into above equation yields

$$C_D = 2 \frac{L_{b+s}}{L_s} \frac{Dg}{\beta v_{\text{term}}^2}, \quad (23)$$

The computed drag coefficient C_D as a function of A and M is plotted in Fig. 5.5 for $\gamma = 1.4$.

The terminal Mach number, v_{term}/c_b , is plotted as a function of the Atwood ratio in Fig. 5.6. Here c_b is the sound speed of the heavy material just below the tip of the spike (Fig. 5.6a) or the bottom of the bubble (Fig. 5.6b). We note that the terminal Mach number has a significant dependence on the compressibility M^2 . The data for $D = 10$ and 100 are not included in the plot because these systems did not reach the terminal velocity region at the final computational step. At the termination of these runs, the dimensionless heights which are the ratio of the amplitude of bubble or spike to the wave length are in the range from 1 to 2.5, but the systems are still fully in the free fall regime. The spike and the bubble velocities do become supersonic (relative to the sound speed of the heavy gas) before the final computation step in the $D = 10$ and 100 , $M^2 = 2$ cases. For $D = 100$, $M^2 = 2$ the spike Mach number reaches 2.7, the bubble Mach number reaches 2.3 and they are still growing. However in all cases considered here, the bubble and spike velocities are subsonic relative to the light gas. If the light fluid is a vacuum ($D = \infty$, $A = 1$) then the spike is expected to remain in free fall. This behavior is consistent with the behavior of an incompressible fluid.²¹

A dimensional analysis of the Euler equation shows that the terminal velocity v_{term} of the bubble scales according to equation (3)

$$|v_{\text{term}}| = c_1 (gr)^{\frac{1}{2}}, \quad (24)$$

where c_1 is a function of the fundamental dimensionless parameters D , M and γ alone and r is half wave length, i.e. the radius or half the width of the single mode computation. Fig. 5.7 illustrates the dependence of the constant c_1 on D and M^2 . As

noted above, the systems with high density ratios have not reached the terminal velocity region at the end of the computation. Therefore the terminal velocity can not be determined in these cases. However, the velocity at the last step of the computation provides us with a lower bound for c_1 in these systems. For $D = 5$, $M^2 = .5$, $c_1 > .36$, for $D = 10$, $M^2 = .5$, $c_1 > .46$ and for $D = 5$, $M^2 = 2$, $c_1 > .47$. The data for a two dimensional (from reference 21 and 22) incompressible ($M^2 = 0$), one component ($A = 1$) fluid is also shown in Fig. 5.7. There is an expectation that $c_1 \approx \text{const } A^{\frac{1}{2}}$. In fact for both the linear and free fall regimes, gravity occurs in the form Ag . If this remains the case for the terminal velocity regime in equation (24), then c_1 would be proportional to $A^{\frac{1}{2}}$. Our data indicates that c_1 has a significant dependence on M^2 . Even allowing for an M^2 dependence in the constant of proportionality, the data does not fit this relation particularly well, especially with the inclusion of the lower bounds for systems not in the terminal velocity region.

The interaction of the spike and bubble with waves reflected from the boundaries leads to a slowing down of their motion, and, for motion in a bounded region, defines a further time regime for the fluid motion.

We have made a series of computations sampling the development of the single finger as a function of D . Figs. 5.8-5.10 present plots of the interface, density contours, and pressure contours for $D = 1.5, 10$, and 100 and $M^2 = .5$. Fig. 5.11-12 presents plots of the interface for $D = 2$ and 100 and $M^2 = 2$. Note that the flow is subsonic in Fig. 5.8 and supersonic relative to the heavy gas in the final frame of Fig. 5.12.

Because there are two dimensionless parameters in the formulation of the problem, D and M^2 (with the equation of state held fixed), there should also be two qualitative features in morphology of the fingers in the deeply nonlinear regime, which change in their relative importance as D and M^2 vary. The effect of increasing D is seen in a trend toward a thinner spike and less roll up shed off the edge of its tip. The effect of increasing M^2 leads to the deposit of a strip or trailing filament of material shed off the edge of the tip in contrast to the highly wound up vortices which are observed in the incompressible case. The increase of M^2 leads to a dramatic increase in terminal bubble and spike Mach numbers. For large values of M^2 , a bow shock forms in the front of the bubble and a complex system of shocks

form in the stem of the spike. The present calculations are only moderately supersonic and so the shocks are weak. However, due to the large value of gravity and the exponential stratification of the pressure, the pressure changes very rapidly in a few mesh layers even in the absence of shock waves, so that these weak shocks are not clearly resolved in the present calculations.

B. The Two Body Problem

In Fig. 5.13-14 we show a series of frames which give the time development of a bubble merger. The parameters for this solution are $D = 2, 10$ and $M^2 = 2$. A detailed study of the two body problem would be an interesting topic for future work, and is required to complete the determination of the parameters in the Sharp-Wheeler model and their dependence on the dimensionless parameters D and M^2 of the compressible Rayleigh-Taylor problem from first principles. In any case we believe that the preliminary result reported here indicates that this goal is feasible, using the front tracking method.

C. Heterogeneity

Heterogeneity can have an important effect on solutions. This is evident from our study⁷ of the incompressible Rayleigh-Taylor problem. A detailed analysis of this topic is postponed to a subsequent paper, but for the present we observe that heterogeneity in the form of turbulence in the flow field could lead to pinch off of the spike or of the trailing edge of the spike roll up, as well as the break up of the spike into droplets. Any of these phenomena would effect the drag coefficient and thus the terminal velocity of the spike. We expect that renormalized gravity, which characterizes the free fall regime, should be less sensitive to heterogeneity.

These preliminary results also suggest additional phenomena, such as bubble pinch off, true multiphase flow and a possible variety of multiphase flow regimes. The bubble mergers presented here actually suggest the regime of slug flow, which is recognized as a regime in the multiphase flow of fluids in pipes. In addition there is good reason to suppose that neighboring bubbles influence one another. For example, two large and neighboring bubbles might have a collective terminal velocity which is larger than either would have individually. The extent and importance of

such additional phenomena is left to further studies as is the task of modifying as necessary the statistical model for bubble merger.

VI. VALIDATION OF SINGLE FINGER COMPUTATIONS

In the small amplitude regime, the computed solution can be compared to the analytic solution, derived in the Appendix, of the linearized equations, where the finger is considered as a small amplitude perturbation of the flat interface. At any amplitude, mesh refinement produces a validation test of the solution. In addition we have determined that the solution is independent of various numerical parameters which adjust the algorithm, and some of these results are presented here. In particular, we study the effect of the initial amplitude of the perturbation, the effect of the boundary condition at the top and bottom of the computational domain and the effect of the remeshing (redistribution) of points along the interface.

We study first the effect of mesh refinement. Obviously the finer the mesh which is used, the greater is the level of detail which one can see. Convergence occurs in the sense that structures which occur on the coarse grid are duplicated on the fine grid. In Fig. 6.1 we illustrate mesh refinement by a factor of 4 in each linear dimension. We note that the degree of resolution we obtain could not be achieved on comparable grids without the use of interface methods. In this figure $D=10$ and $M^2=0.5$. As we see in Fig. 6.2, the positions of the spike and the bubble are not very sensitive to mesh refinement. The reason is that convergence for these features of the solution has largely occurred on the coarse grid, and so the mesh refinement only affects the detailed structure of the interface and in particular the secondary instabilities on the side of the spike. Secondary structures, which occur on the finest grid only, as in Fig. 5.9 and Fig. 6.1 are not confirmed by the validation studies presented here. They are somewhat sensitive to numerical parameters such as frequency of remeshing; frequent remeshing of the interface is equivalent to smoothing and tends to suppress these secondary structures. We anticipate that the secondary structures also depend sensitively on surface physics effects, such as surface tension or a viscous diffusion layer.

In the small amplitude region, the interface is smooth and nearly flat. In that region, the spike and bubble grow exponentially. We define a dimensionless

amplitude, a , the ratio of the initial perturbation amplitude at the interface to the wave length. In order to test carefully the computation in the linear regime, we start at a very small value of a , $a = 0.001$, in Fig. 6.3 and show the comparison of the bubble and spike velocity and the position for the linear theory and the full Euler equations. In Fig. 6.4, we have plotted the velocity and the position of the bubble starting with two different values of a , $a = .004$ and $a = .01$, superimposed. As we can see from the figure, the end of the linear regime and the behavior of the system after exit from the linear regime are independent of the initial starting amplitude provided that this amplitude lies in the linear region. In the study of the nonlinear regime, it is desirable to start the initial amplitude as large as possible to minimize the effects of the reflected wave from the boundary, which we will discuss in Fig. 6.6.

Because of the agreement between the computed solution and the linear theory and between the computed solutions with different starting amplitudes, we believe that the initial amplitude and the linear ansatz in the initialization of the computed solution have no effect on the computation. Furthermore, we see that the linear theory gives good agreement up to amplitudes $a = 0.015$ and so these values of initial a are used in the further studies of the nonlinear regime.

In the small amplitude regime, the interface is smooth and nearly flat. Therefore the remeshing of the interface is not required, and its only effect is a regularization through interpolation. Thus we see in Fig. 6.5 that remeshing at a low frequency (once per 15 or once per 100 time steps) has no influence on growth rates, while a remeshing every time step has the expected effect of lowering the growth rate of the instability. Furthermore a frequent remeshing suppresses the secondary instabilities on the surface of the spike.

For small times, the upper and lower boundaries have no effect on the motion of the interface due to the finite propagation speed. In the free fall regime, we have observed that the effect of the reflected boundary signals is not very strong. In the terminal velocity region, reflected boundary signals can have a very noticeable effect on the interface. In Fig. 6.6, we compare the bubble position and velocity for a domain of shape 1×4 and 1×8 . At late times the boundary signals do effect the terminal velocity. The times marked by an arrow show the first arrival of a signal

from the nearest boundary and the first arrival of a reflected signal starting initially at the interface. The first of these times marks the beginning of a quantitative divergence between these two curves and the second marks the beginning of a qualitative difference, with the boundary reflected signal causing the velocity to begin decreasing in magnitude in the shorter region. The other anomalies in the velocity vs time plots are coarse mesh phenomena, and clearly have nothing to do with boundary effects, as can be seen by the fact that they occur at the same locations for the two runs with different boundary locations. To further emphasize this point we also plot in this figure a finer grid computation of the same quantities for the shorter domain.

At large time, it is necessary to remesh the interface due to the large scale distortions in the geometry. It seems that remeshing at on the order of at least every 20 time steps is required. If the interface is remeshed more frequently, then the secondary structure of the surface waves on the side of the spike are suppressed but the position of the bubble and spike is not greatly affected. For the extreme case of remeshing every time step, however, the growth rates of the bubble and spike are affected, as we have seen.

ACKNOWLEDGMENTS

This work is supported in part by the Applied Mathematical Sciences subprogram, U. S. Department of Energy, contract DE-AC02-76ER03077 (C. L. Gardner, J. Glimm, O. McBryan and Q. Zhang), the National Science Foundation, grant DMS-83-1229 (J. Glimm and O. McBryan), the Army Research Organization, grant DAAG29-85-K-0188 (J. Glimm), and the U. S. Department of Energy (R. Menikoff and D. H. Sharp).

APPENDIX: THE LINEARIZED COMPRESSIBLE RAYLEIGH-TAYLOR THEORY

We derive the equations governing the initialization of the single-mode Rayleigh-Taylor computations. Although our derivation is given explicitly for the single-mode problem, the solutions for the multiple-mode Rayleigh-Taylor computations can be obtained by the superposition of the single-mode solutions, since the equations are linear and different modes do not couple with each other at this order.

Our analysis extends results of ref. 19.

The two-dimensional Euler equations for a compressible, inviscid, gas are

$$\frac{\partial \rho}{\partial t} + \frac{\partial \rho u}{\partial x} + \frac{\partial \rho v}{\partial z} = 0 \quad (\text{A1})$$

$$\frac{\partial \rho u}{\partial t} + \frac{\partial (\rho u^2 + P)}{\partial x} + \frac{\partial \rho u v}{\partial z} = 0 \quad (\text{A2})$$

$$\frac{\partial \rho v}{\partial t} + \frac{\partial \rho u v}{\partial x} + \frac{\partial (\rho v^2 + P)}{\partial z} = \rho g \quad (\text{A3})$$

$$\frac{\partial}{\partial t} [\rho (\frac{1}{2} q^2 + e)] + \frac{\partial}{\partial x} [\rho u (\frac{1}{2} q^2 + i)] + \frac{\partial}{\partial z} [\rho v (\frac{1}{2} q^2 + i)] = \rho v g, \quad (\text{A4})$$

where u is the x component of the velocity, v is the z component of the velocity, $q^2 = u^2 + v^2$, e is the specific internal energy and

$$i = e + \frac{P}{\rho} \quad (\text{A5})$$

is the specific enthalpy. The thermodynamic quantities pressure and density are related by the equation of state,

$$e = e(p, \rho). \quad (\text{A6})$$

Suppose we have a perfect flat interface between the light gas (above a) and the heavy gas (below b). This isothermal equilibrium state is determined from the following equations:

$$\frac{\partial P_0}{\partial z} = \rho_0 g \quad (\text{A7})$$

$$\frac{\partial}{\partial z} (e_0 + \frac{P_0}{\rho_0}) = 0 \quad (\text{A8})$$

$$e_0 = e(P_0, \rho_0). \quad (\text{A9})$$

Here the subscript zero represents the solutions of the isothermal equilibrium state, and gravitation is taken to point in the positive z direction.

To analyze the Rayleigh-Taylor instability, we imagine that the interface between the light and the heavy gas is perturbed as a sine wave with one mode. Since the perturbation is small, the state of the system should be close to the solution of the isothermal equilibrium state on the short time scale. Therefore to linearize the equations (A1)–(A4) and (A6), we write each function as its zeroth order (equilibrium)

solution and a first order correction,

$$\rho \approx \rho_0 + \delta\rho \quad (\text{A10})$$

$$P \approx P_0 + \delta P \quad (\text{A11})$$

$$u \approx \delta u \quad (\text{A12})$$

$$v \approx \delta v \quad (\text{A13})$$

$$e \approx e_0 + \delta e. \quad (\text{A14})$$

Here we have used the results that the zeroth order solutions for velocities in the x and z direction, u_0 and v_0 , are zero. The linearized equations are

$$\frac{\partial \delta \rho}{\partial t} + \rho_0 \frac{\partial \delta u}{\partial x} + \rho_0 \frac{\partial \delta v}{\partial z} + \frac{\partial \rho_0}{\partial z} \delta v = 0 \quad (\text{A15})$$

$$\rho_0 \frac{\partial \delta u}{\partial t} + \frac{\partial \delta P}{\partial x} = 0 \quad (\text{A16})$$

$$\rho_0 \frac{\partial \delta v}{\partial t} + \frac{\partial \delta P}{\partial z} = g \delta \rho \quad (\text{A17})$$

$$\begin{aligned} e_0 \frac{\partial \delta \rho}{\partial t} + \rho_0 \frac{\partial \delta e}{\partial t} + \rho_0 i_0 \frac{\partial \delta u}{\partial x} + \rho_0 i_0 \frac{\partial \delta v}{\partial z} + i_0 \frac{\partial \rho_0}{\partial z} \delta v \\ + \rho_0 \frac{\partial i_0}{\partial z} \delta v = \rho_0 g \delta v \end{aligned} \quad (\text{A18})$$

$$\frac{\partial \delta e_0}{\partial t} = \frac{\partial e_0}{\partial \rho_0} \frac{\partial \delta \rho}{\partial t} + \frac{\partial e_0}{\partial P_0} \frac{\partial \delta P}{\partial t}. \quad (\text{A19})$$

By using equations (A5), (A8), (A15) and (A19), equation (A18) can be rewritten as

$$\left(\rho_0 \frac{\partial e_0}{\partial \rho_0} - \frac{P_0}{\rho_0} \right) \frac{\partial \delta \rho}{\partial t} + \rho_0 \frac{\partial e_0}{\partial P_0} \frac{\partial \delta P}{\partial t} = \rho_0 g \delta v. \quad (\text{A20})$$

Since all the coefficients are the functions of z , we can write each function as

$$\delta f_i = \exp(\sigma t + i k x) \delta \tilde{f}_i(z), \quad (\text{A21})$$

for $\delta f_i = \delta \rho, \delta P, \delta u, \delta v$. Here $\delta \tilde{f}_i$ is a function only of z . Each value of σ and k corresponds a single mode. By using equation (A21), the linearized equations become

$$\sigma \delta \tilde{\rho} + i k \rho_0 \delta \tilde{u} + \rho_0 \frac{d \delta \tilde{v}}{dz} + \frac{\partial \rho_0}{\partial z} \delta \tilde{v} = 0 \quad (\text{A22})$$

$$\sigma \rho_0 \delta \tilde{u} + i k \delta \tilde{P} = 0 \quad (\text{A23})$$

$$\sigma \rho_0 \delta \bar{v} + \frac{d\delta \bar{P}}{dz} = g \delta \bar{\rho} \quad (\text{A24})$$

$$\sigma \left(\rho_0 \frac{\partial e_0}{\partial \rho_0} \delta \bar{\rho} - \frac{P_0}{\rho_0} \right) + \sigma \rho_0 \frac{\partial e_0}{\partial P_0} \delta \bar{P} = \rho_0 g \delta \bar{v}. \quad (\text{A25})$$

After eliminating the functions $\delta \bar{u}$ and $\delta \bar{v}$, we have two equations for the functions $\delta \bar{\rho}$ and $\delta \bar{P}$,

$$\sigma^2 \delta \bar{\rho} + g \frac{d}{dz} \delta \bar{\rho} + k^2 \delta \bar{P} - \frac{d^2}{dz^2} \delta \bar{P} = 0 \quad (\text{A26})$$

$$\sigma^2 \left(\rho_0 \frac{\partial e_0}{\partial \rho_0} - \frac{P_0}{\rho_0} - \frac{g^2}{\sigma^2} \right) \delta \bar{\rho} + \sigma^2 \rho_0 \frac{\partial e_0}{\partial P_0} \delta \bar{P} + g \frac{d}{dz} \delta \bar{P} = 0. \quad (\text{A27})$$

Finally, we obtain a second order ordinary differential equation for $\delta \bar{P}$,

$$C_2(z) \frac{d^2 \delta \bar{P}}{dz^2} + C_1(z) \frac{d\delta \bar{P}}{dz} + C_0(z) \delta \bar{P} = 0, \quad (\text{A28})$$

where

$$C_2(z) = \left(\rho_0 \frac{\partial e_0}{\partial \rho_0} - \frac{P_0}{\rho_0} \right) \left(\rho_0 \frac{\partial e_0}{\partial \rho_0} - \frac{P_0}{\rho_0} - \frac{g^2}{\sigma^2} \right)^{-1} \quad (\text{A29})$$

$$C_1(z) = g \left(\rho_0 \frac{\partial e_0}{\partial P_0} + 1 \right) \left(\rho_0 \frac{\partial e_0}{\partial \rho_0} - \frac{P_0}{\rho_0} - \frac{g^2}{\sigma^2} \right)^{-1} + \frac{g^2}{\sigma^2} \frac{d}{dz} \left(\rho_0 \frac{\partial e_0}{\partial \rho_0} - \frac{P_0}{\rho_0} - \frac{g^2}{\sigma^2} \right)^{-1} \quad (\text{A30})$$

$$C_0(z) = \sigma^2 \rho_0 \frac{\partial e_0}{\partial P_0} \left(\rho_0 \frac{\partial e_0}{\partial \rho_0} - \frac{P_0}{\rho_0} - \frac{g^2}{\sigma^2} \right)^{-1} + g \frac{d}{dz} \left[\rho_0 \frac{\partial e_0}{\partial P_0} \left(\rho_0 \frac{\partial e_0}{\partial \rho_0} - \frac{P_0}{\rho_0} - \frac{g^2}{\sigma^2} \right)^{-1} \right] - k^2. \quad (\text{A31})$$

Once this equation can be solved, all the other three functions can be obtained from $\delta \bar{P}$. $\delta \bar{\rho}$ can be obtained from equation (A27), $\delta \bar{u}$ from equation (A23) and $\delta \bar{v}$ from equation (A24). These equations hold for the light and heavy fluid separately. They are coupled together by the boundary conditions at their interface; namely, that the pressure P and normal velocity are continuous to first order in $\delta \bar{v}$. This determines the growth rate σ .

To illustrate our results, we assume our system is a stiffened polytropic gas²³ The specific internal energy for a stiffened polytropic gas is

$$e = \frac{(P + \gamma P_s)}{(\gamma - 1)\rho}, \quad (\text{A32})$$

where γ is a dimensionless constant and P_s is a constant with the dimension of pressure. The unperturbed gases are in exponentially stratified isothermal equilibrium:

$$\rho_a = \rho_{a0} \exp(\beta_a(z - z_{\text{intfc}})) \quad (\text{A33})$$

$$\rho_b = \rho_{b0} \exp(\beta_b(z - z_{\text{intfc}})) \quad (\text{A34})$$

where z_{intfc} is the z position of the unperturbed interface, $\beta = \frac{\gamma g}{c^2}$ and

$$c = \left[\frac{\gamma(P + P_s)}{\rho} \right]^{\frac{1}{2}}.$$

We suppose that the position η of the perturbed interface is given by $\eta - z_{\text{intfc}} = A_{\text{init}} \exp(\sigma t) \sin(kx)$, where σ is the growth rate of the surface and k is the wave number of the perturbation and A_{init} is the amplitude of the perturbation at interface at time $t = 0$. We assume that the problem is periodic in x with reflecting boundaries at $z = z_{\text{bdry}}$, where z_{bdry} is the top (bottom) of the computational domain.

The linearized Euler equations (A15)–(A18) become

$$\sigma \delta \bar{p} + ik \rho_0 \delta \bar{u} + \rho_0 \frac{\partial \delta \bar{v}}{\partial z} + \beta \rho_0 \delta \bar{v} = 0 \quad (\text{A35})$$

$$\sigma \rho_0 \delta \bar{u} = -ik \delta \bar{P} \quad (\text{A36})$$

$$\sigma \rho_0 \delta \bar{v} + \frac{\partial \delta \bar{P}}{\partial z} = g \delta \rho \quad (\text{A37})$$

$$\sigma \delta \bar{P} + \beta(P_0 + P_s) \delta \bar{v} + \gamma(P_0 + P_s) \left(ik \delta \bar{u} + \frac{\partial \delta \bar{v}}{\partial z} \right) = 0, \quad (\text{A38})$$

and equation (A28) becomes

$$\frac{\partial^2 \delta \bar{P}}{\partial z^2} - \frac{\gamma g}{c^2} \frac{\partial \delta \bar{P}}{\partial z} - \left[\frac{\sigma^2}{c^2} + k^2 + \frac{(\gamma - 1)g^2 k^2}{\sigma^2 c^2} \right] \delta \bar{P} = 0. \quad (\text{A39})$$

Now assume

$$\delta \bar{P} \sim \exp\left((\alpha + \beta)(z - z_{\text{intfc}})\right) \quad (\text{A40})$$

$$\delta \bar{p} \sim \exp\left((\alpha + \beta)(z - z_{\text{intfc}})\right), \quad (\text{A41})$$

while

$$\delta \tilde{u}, \delta \tilde{v} \sim \exp(\alpha(z - z_{\text{intfc}})). \quad (\text{A42})$$

From equation (A39),

$$\alpha_{\pm} = -\frac{\gamma g}{2c^2} \pm \left[\frac{\gamma^2 g^2}{4c^4} + \frac{\sigma^2}{c^2} + k^2 + \frac{(\gamma - 1)g^2 k^2}{c^2 \sigma^2} \right]^{\frac{1}{2}}. \quad (\text{A43})$$

We impose the boundary conditions $\delta v(z = z_{\text{bdry}}) = 0$. The solution of the linearized Euler equations is then

$$\begin{aligned} \delta P = & -\frac{(\gamma - 1)g^2 + c^2 \sigma^2}{\exp(\alpha_-(z_{\text{intfc}} - z_{\text{bdry}})) - \exp(\alpha_+(z_{\text{intfc}} - z_{\text{bdry}}))} \rho_0 A \times \\ & \left[\frac{\exp(\alpha_-(z - z_{\text{bdry}}))}{(\gamma - 1)g + \alpha_- c^2} - \frac{\exp(\alpha_+(z - z_{\text{bdry}}))}{(\gamma - 1)g + \alpha_+ c^2} \right] \times \\ & \exp(\sigma t + ikx) \exp(\beta(z - z_{\text{intfc}})), \end{aligned} \quad (\text{A44})$$

$$\delta \rho = \frac{-1}{(\gamma - 1)g^2 + c^2 \sigma^2} [\sigma^2 \delta P + (\gamma - 1)g \frac{d}{dz} \delta P], \quad (\text{A45})$$

$$\delta v = \frac{1}{\sigma \rho_0} (g \delta \rho - \frac{d}{dz} \delta P), \quad (\text{A46})$$

$$\delta u = \frac{-ik}{\sigma \rho_0} \delta P. \quad (\text{A47})$$

Note that $\delta v(z = z_{\text{intfc}}) = \sigma A \exp(\sigma t + ikx)$ is continuous at the interface. The growth rate σ is determined from the condition

$$\delta P_+ - \delta P_- = \left(\frac{\partial P}{\partial z_-} - \frac{\partial P}{\partial z_+} \right) A = (\rho_b - \rho_a) g A \quad (\text{A48})$$

which expresses the continuity of the pressure at the interface

$$P_+(z_{\text{intfc}} + \eta) + \delta P_+ = P_-(z_{\text{intfc}} + \eta) + \delta P_-. \quad (\text{A49})$$

Here the subscripts $+$ ($-$) denote variables evaluated just above (below) the interface. We find

$$\begin{aligned} (\rho_b - \rho_a)g = & -\frac{(\gamma - 1)g^2 + c_a^2 \sigma^2}{\exp(\alpha_a-(z_{\text{intfc}} - z_{\text{bdry}})) - \exp(\alpha_a+(z_{\text{intfc}} - z_{\text{bdry}}))} \times \\ & \rho_a \left[\frac{\exp(\alpha_a-(z_{\text{intfc}} - z_{\text{bdry}}))}{(\gamma - 1)g + \alpha_a - c_a^2} - \frac{\exp(\alpha_a+(z_{\text{intfc}} - z_{\text{bdry}}))}{(\gamma - 1)g + \alpha_a + c_a^2} \right] \end{aligned}$$

$$+ \frac{(\gamma - 1)g^2 + c_b^2 \sigma^2}{\exp(\alpha_b - (z_{intfc} - z_{bdry})) - \exp(\alpha_b + (z_{intfc} - z_{bdry}))} \times$$

$$\rho_b \left[\frac{\exp(\alpha_b - (z_{intfc} - z_{bdry}))}{(\gamma - 1)g + \alpha_b - c_b^2} - \frac{\exp(\alpha_b + (z_{intfc} - z_{bdry}))}{(\gamma - 1)g + \alpha_b + c_b^2} \right] \quad (A50)$$

- ¹D. H. Sharp and J. A. Wheeler. Late Stage of Rayleigh-Taylor Instability. Institute for Defense Analyses. Unpublished Report, 1961.
- ²I. L. Chern, J. Glimm, O. McBryan, B. Plohr and S. Yaniv. J. Comp. Phys., **62** 83-110 (1986).
- ³C. Fithian and C. L. Gardner In Preparation.
- ⁴C. L. Gardner. Phys. of Fluids., **29** 690-695 (1986).
- ⁵J. Glimm, Eli Isaacson, D. Marchesin and O. McBryan. Adv. Appl. Math. **2** 91-119 (1981).
- ⁶J. Glimm, C. Klingenberg, O. McBryan, B. Plohr, D. H. Sharp and S. Yaniv. Adv. Appl. Math., **6** 259-290 (1985).
- ⁷J. Glimm, O. McBryan, R. Menikoff and D. H. Sharp. SIAM J. Sci. Stat. Computing. **7** 230-251, (1986).
- ⁸D. L. Youngs. Physica **12d** 32-44 (1984).
- ⁹B. Kashiwa and R. Mjolsness. Los Alamos National Laboratory Technical Report LA-10307-MS.
- ¹⁰G. Wallis. One-dimensional Two Phase Flow. McGraw-Hill, New York 1969.
- ¹¹G. Papanicolaou, ed. Advances in Multiphase Flow and Related Problems. SIAM, Philadelphia 1987.
- ¹²C. P. Verdon, R. L. McCrory, R. L. Morse, G. R. Baker, D. I. Meiron and S. A. Orszag. Phys. of Fluids **25** 1653-1674 (1982).
- ¹³C. E. Leith. Instability Notes II: A Bubble Growth Model for Final Stage Multiple Scale Rayleigh-Taylor Instability in Two Dimensions. Preprint Mar. 1984.
- ¹⁴K. I. Read. Physica **12D** 45 (1984).

- ¹⁵J. Glimm, O. McBryan, R. Menikoff and D. H. Sharp. To be published.
- ¹⁶J. Glimm. In: *Advances in Multiphase Flow and Related Problems*. SIAM, Philadelphia 1987 (Ed.: G. Papanicolaou).
- ¹⁷C. Gardner, J. Glimm, J. Grove, O. McBryan, R. Menikoff, D. H. Sharp and Q. Zhang. To appear in *Physics D*.
- ¹⁸D. H. Sharp. *Physica* **12d** 3-18 (1984).
- ¹⁹I. B. Bernstein and D. L. Book. *Phys. of Fluids* **26** 453-458 (1983).
- ²⁰G. K. Batchelor. *An Introduction to Fluid Dynamics*. Cambridge University Press. Cambridge, 1967, p.337.
- ²¹R. Menikoff and C. Zemach, *J. Comp. Phys.* **51** 28 (1983).
- ²²G. R. Baker, D. I. Meiron and S. A. Orszag. *Phys. of Fluids* **23** 1485-1490 (1980).
- ²³F. Harlow and A. Amsden, LANL Monograph LA-4700 (1971)

FIGURE CAPTIONS

Fig. 4.1 The location in x, t space of bubble mergers. (H) corresponds to the run H , and (L) corresponds to run L .

Fig. 4.2H *bubble radial distribution vs. $\ln(r)$ for run H at a sequence of times.*

Fig. 4.2L *bubble radial distribution vs. $\ln(r)$ for run L at a sequence of times.* Different scales are used between the ranges from 0 to 60 and from 60 to 5200 in the y direction in order to display both the large cluster of bubbles near $r = r_0$ and the remainder of the distribution.

Fig. 4.3 *$\ln(\text{number of bubbles})$ vs. time.* (H) corresponds to run H , and (L) corresponds to run L .

Fig. 4.4 *average velocity vs. time.* (H) corresponds to run H , and (L) corresponds to run L . The derivative of the velocity versus time in (L) is about 7 times larger than the derivative in (H).

Fig. 4.5 *\log of minimum, mean and maximum bubble radius vs. time.* (H) corresponds to run H , and (L) corresponds to run L .

Fig. 4.6 $\ln(r_{\max}/r_{\text{mean}})$ vs. time. (H) corresponds to run H, and (L) corresponds to run L.

Fig. 4.7 minimum, mean and maximum bubble height vs. time. (H) corresponds to run H, and (L) corresponds to run L.

Fig. 4.8 radius, height cross correlation vs. time. (H) corresponds to run H, and (L) corresponds to run L.

Fig. 4.9 radius and height correlation vs. time. (H) corresponds to run H, and (L) corresponds to run L.

Fig. 4.10 The expected scaled radii \bar{r}_c and height \bar{h}_c of bubbles adjacent to large bubbles are plotted as a function of time. The y axis is in units of dimensionless length. This plot should be contrasted to Fig. 4.5 and Fig. 4.7, which display mean radius and height without restriction.

Fig. 5.1 The dependence of the dimensionless growth rate on A and M^2 . The difference between two adjacent constant contours is 0.793.

Fig. 5.2. Plots of spike velocity and bubble velocity versus time are shown with the best two parameter fit to equation (21) superimposed, for the parameter values $D = 2$, $M^2 = 0.5$, $\gamma = 1.4$. The numerical results are obtained by using a 80 by 640 grid in a computational domain 1×8 .

Fig. 5.3 The comparison of the spike velocity and the spike acceleration of the numerical result to its linear and large time asymptotic behavior for $D = 2$, $M^2 = .5$ and $\gamma = 1.4$. The solid lines are the numerical results obtained by using a 80 by 640 grid in a computational domain 1×8 .

Fig. 5.4 The plots of the renormalization factor for gravity versus the Atwood ratio for (a) spike and (b) bubble. For comparison, the straight lines which are proportional to the Atwood ratio are also plotted. The data for a one component, incompressible fluid ($A = 1$, $M^2 = 0$) is taken from reference 20.

Fig. 5.5 The plot of the spike drag coefficient C_D versus the Atwood ratio for $M^2 = .5$ (+) and 2 (x) and $\gamma = 1.4$. Note that for $A = 1$, $C_D = 0$ on theoretical grounds and this suggests an empirical relation $C_D = \text{const} (1 - A)$ with the constant dependent on M .

Fig. 5.6 Plots of Mach number (the ratio of the terminal velocity to the sound speed of the heavy gas) of (a) spike and (b) bubble versus the Atwood ratio. The high density ratio systems have not reached the terminal velocity region at the end of the computation. Therefore the terminal velocity can not be determined in these systems. The spike and the bubble velocities at the last computation step are supersonic (relative to the sound speed of the heavy gas) in the $D = 10$ and 100 cases. In the incompressible case ($M^2 = 0$), $|v_{\text{term}}/c| = 0$ by definition.

Fig. 5.7 A plot of the constant c_1 versus the square root of the Atwood ratio for $D = 2$ and 3 , $M^2 = .5$ (+), 2 (×), and $\gamma = 1.4$. The values of c_1 calculated from the two (* and Δ) dimensional incompressible ($M^2 = 0$, $A = 1$) theories are also shown. The value for (*) comes from reference 21 and (Δ) comes from reference 22.

Fig. 5.8 Plots of the interface position, density and pressure contours for $D = 1.5$, $M^2 = .5$, $a = .015$, $\gamma = 1.4$ in a computation domain 1×6 with a 40 by 240 grid. Only the upper two thirds of the computational region is shown in the plot because nothing of interest occurs in the remainder of the computation. (a) The interface position for successive time steps. (b) The density contour plot. (c) The pressure contour plot.

Fig. 5.9 Plots of the interface position, density and pressure contours for $D = 10$, $M^2 = .5$, $a = .015$, $\gamma = 1.4$ in a computation domain 1×4 with a 40 by 160 grid. (a) The interface position for successive time steps. (b) The density contour plot. (c) The pressure contour plot.

Fig. 5.10 Plots of the interface position, density and pressure contours for $D = 100$, $M^2 = .5$, $a = .015$, $\gamma = 1.4$ in a computation domain 1×10 with a 20 by 200 grid. Only the upper four fifths of the computational region is shown in the plot because nothing of interest occurs in the remainder of the computation. (a) The interface position for successive time steps. (b) The density contour plot. (c) The pressure contour plot.

Fig. 5.11 Plots of the interface position, density and pressure contours for $D = 2$, $M^2 = 2$, $a = .015$, $\gamma = 1.4$ in a computation domain 1×8 with a 80 by 640 grid. Only the middle portion of the computational region is shown in the plot because nothing of interest occurs in the remainder of the computation.

Fig. 5.12 Plots of the interface position, density and pressure contours for $D = 100$, $M^2 = 2$, $a = .015$, $\gamma = 1.4$ in a computation domain 1×6 with a 20 by 120 grid. (a) The interface position for successive time steps. (b) The density contour plot. (c) The pressure contour plot.

Fig. 5.13 Plots of the interface position, density and pressure contours of a bubble merger for $D = 2$, $M^2 = 2$, $\gamma = 1.4$ in a computation domain 1×4 with a 75 by 300 grid. (a) The interface position for successive time steps. (b) The density contour plot. (c) The pressure contour plot.

Fig. 5.14 Plots of the interface position, density and pressure contours of a bubble merger for $D = 10$, $M^2 = 2$, $\gamma = 1.4$ in a computation domain 1×4 with a 75 by 300 grid. (a) The interface position for successive time steps. (b) The density contour plot. (c) The pressure contour plot.

Fig. 6.1 Positions of the front at a sequence of time steps for $D = 10$, $M^2 = 0.5$ and $a = 0.015$ by using 40 by 160 and 10 by 40 grids. The finer grids resolve the more detailed structure of the interface.

Fig. 6.2 A comparison of the position of the spike and the bubble for $D = 10$, $M^2 = 0.5$ and $a = 0.015$ using (A) 10 by 40, (B) 20 by 80, (C) 40 by 160 and (E) 80 by 320 grids. Plot *a* is the position of the spike. Plot *b* is the position of the bubble. For comparison, the linear theory is also shown. As can be seen, most of the computation is out of the linear regime.

Fig. 6.3 A comparison of the spike and the bubble velocity and position for the linear theory and the full Euler equations. Here $D = 10$, $M^2 = 0.5$ and $a = 0.001$. A 40 by 160 grid was used in a computational region of size 1 by 4.

Fig. 6.4 A comparison of different initial starting amplitudes for $D = 10$, $M^2 = 0.5$, $a = 0.004$ and $A = 0.01$ using a 40 by 320 grid in a computational region of size 1 by 4. The time plot is terminated at $t = 4$ because for $a = 0.004$, the one way reflected waves in the heavy gas arrive at the interface shortly after that and the agreement between these two runs does not and should not persist after this time.

Fig. 6.5 A comparison of different redistribution frequencies for $D = 10$, $M^2 = 0.5$ and $a = 0.01$ with a 40 by 160 grid in a computational region of size 1 by 4. $f = 1, 15, 100$ corresponds to redistributing the front every 1, 15, 100 time steps. Plot *a* is for the position of the spike. Plot *b* is for the interface. Compare to frame

2 of Fig. 6.1.

Fig. 6.6 A comparison of boundary effects for a domain of shape 1×4 (A) and 1×8 (B) with 10 by 40 and 10 by 80 grids respectively. Here $D = 10$, $M^2 = 0.5$ and $a = 0.015$. The one way reflected wave corresponds to a signal from the nearest boundary. The two way reflected wave corresponds to a signal starting from the interface. Plot a is for the velocity of the bubble. Plot b is for the position of the bubble. For distinguishing the boundary effects from the grid effects, a 40 by 160 grid curve (A') in the computation domain 1×4 is also plotted as a dotted line in the plot a . The wiggles which are common to A and B (and missing in A') are grid effects, while the divergence between A and B, marked by the arrival of the one way and two way reflected signals are pure boundary effects.

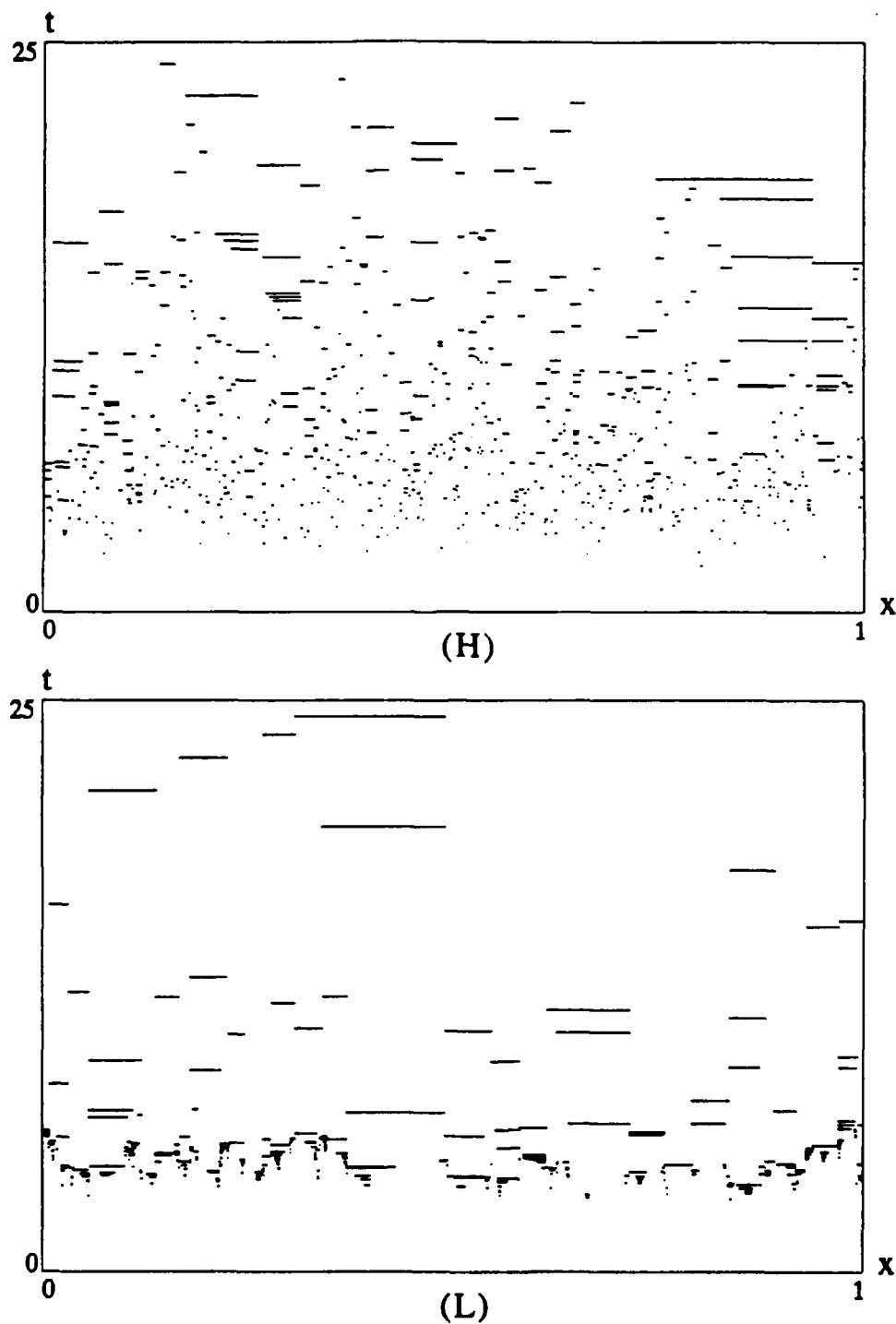


Fig. 4.1 The location in x, t space of bubble mergers. (H) corresponds to the run H , and (L) corresponds to run L .

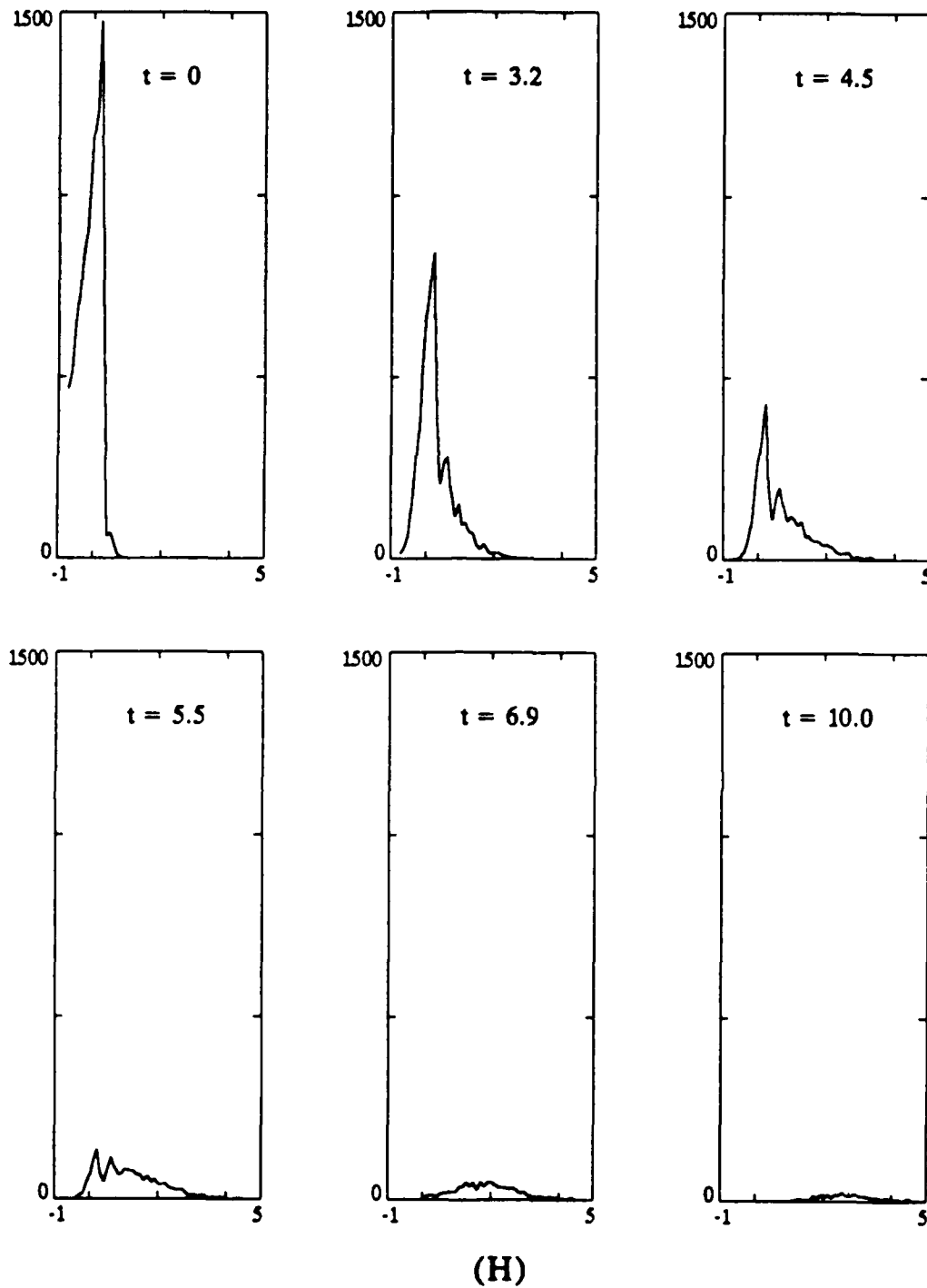


Fig. 4.2H bubble radial distribution vs. $\ln(r)$ for run H at a sequence of times.

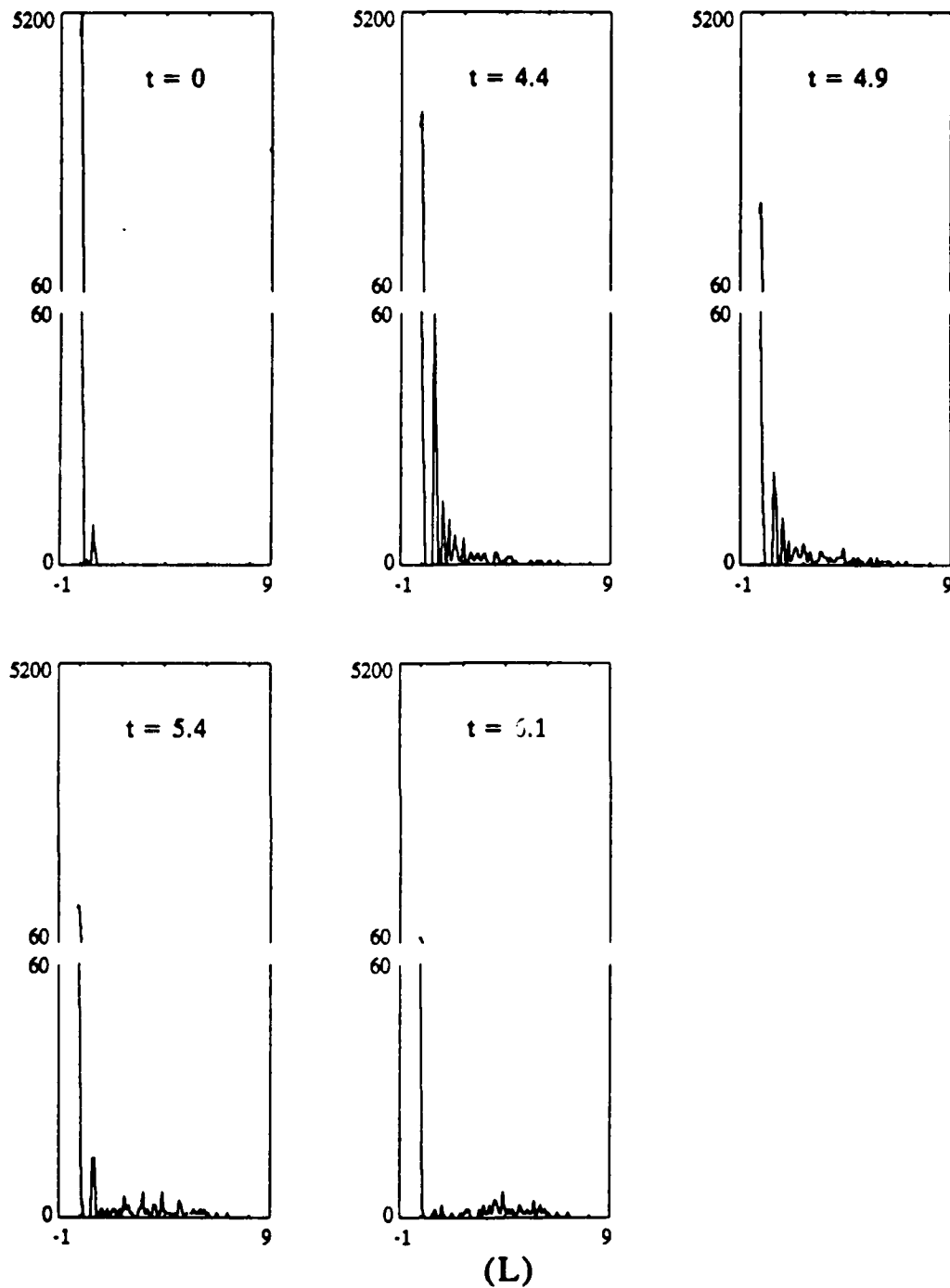


Fig. 4.2L bubble radial distribution vs. $\ln(r)$ for run L at a sequence of times. Different scales are used between the ranges from 0 to 60 and from 60 to 5200 in the y direction in order to display both the large cluster of bubbles near $r = r_0$ and the remainder of the distribution.

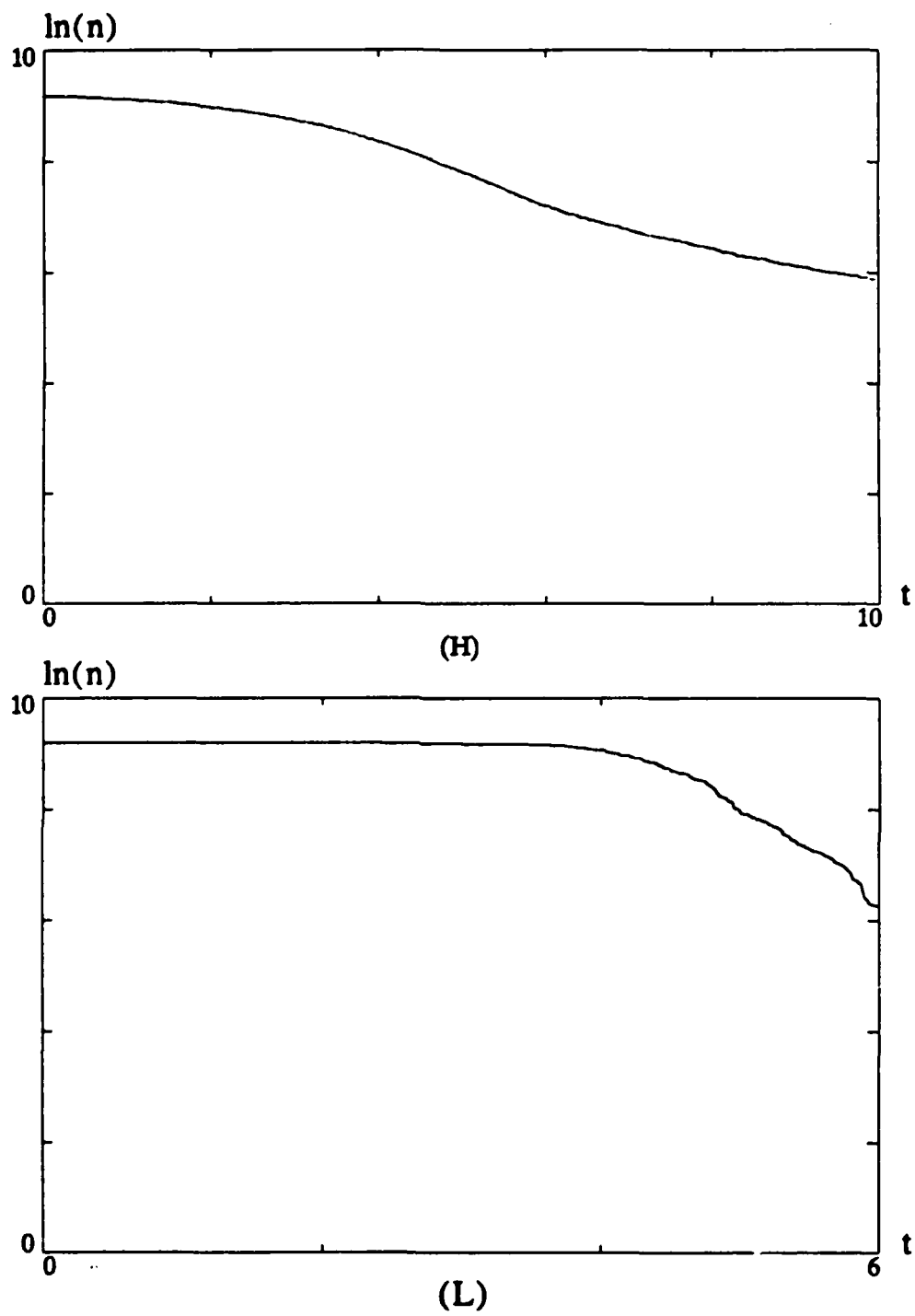


Fig. 4.3 $\ln(\text{number of bubbles})$ vs. time. (H) corresponds to run H, and (L) corresponds to run L.

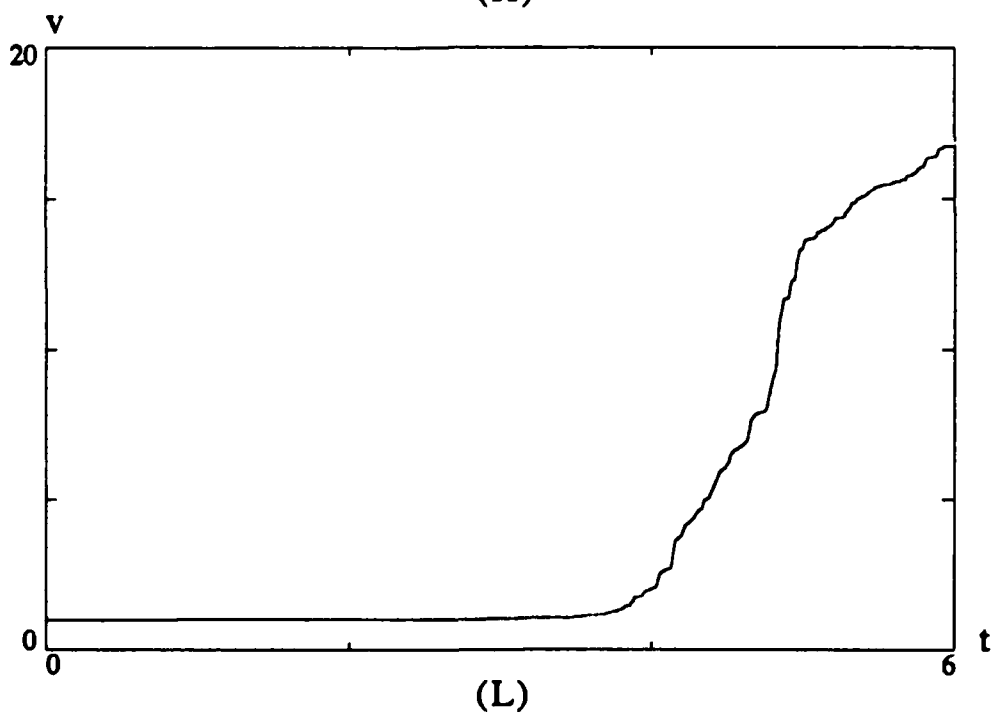
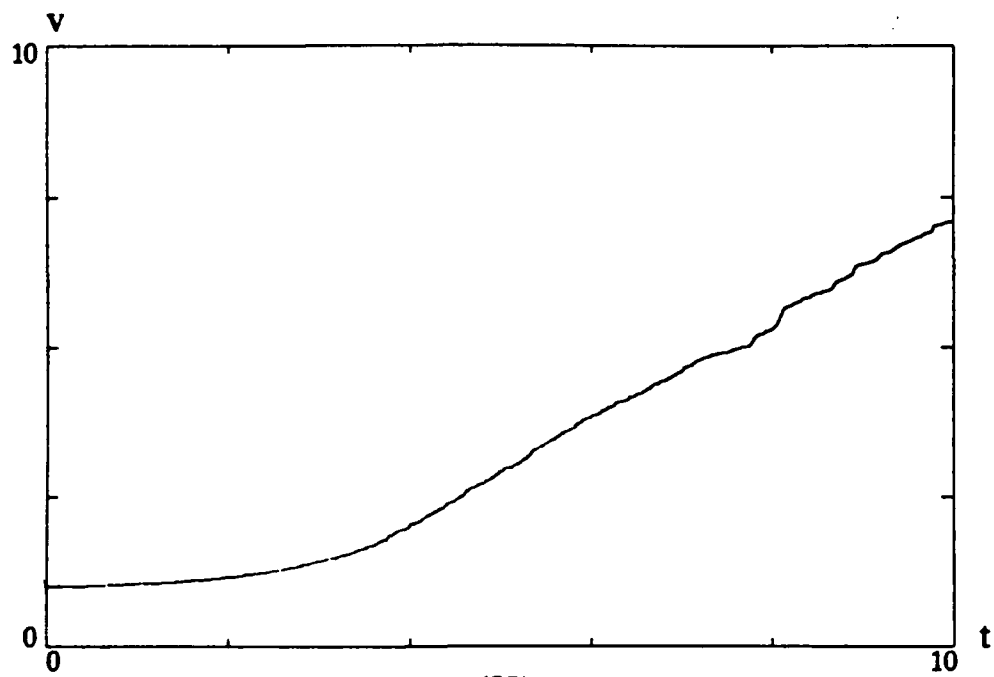


Fig. 4.4 *average velocity vs. time*. (H) corresponds to run H, and (L) corresponds to run L. The derivative of the velocity versus time in (L) is about 7 times larger than the derivative in (H).

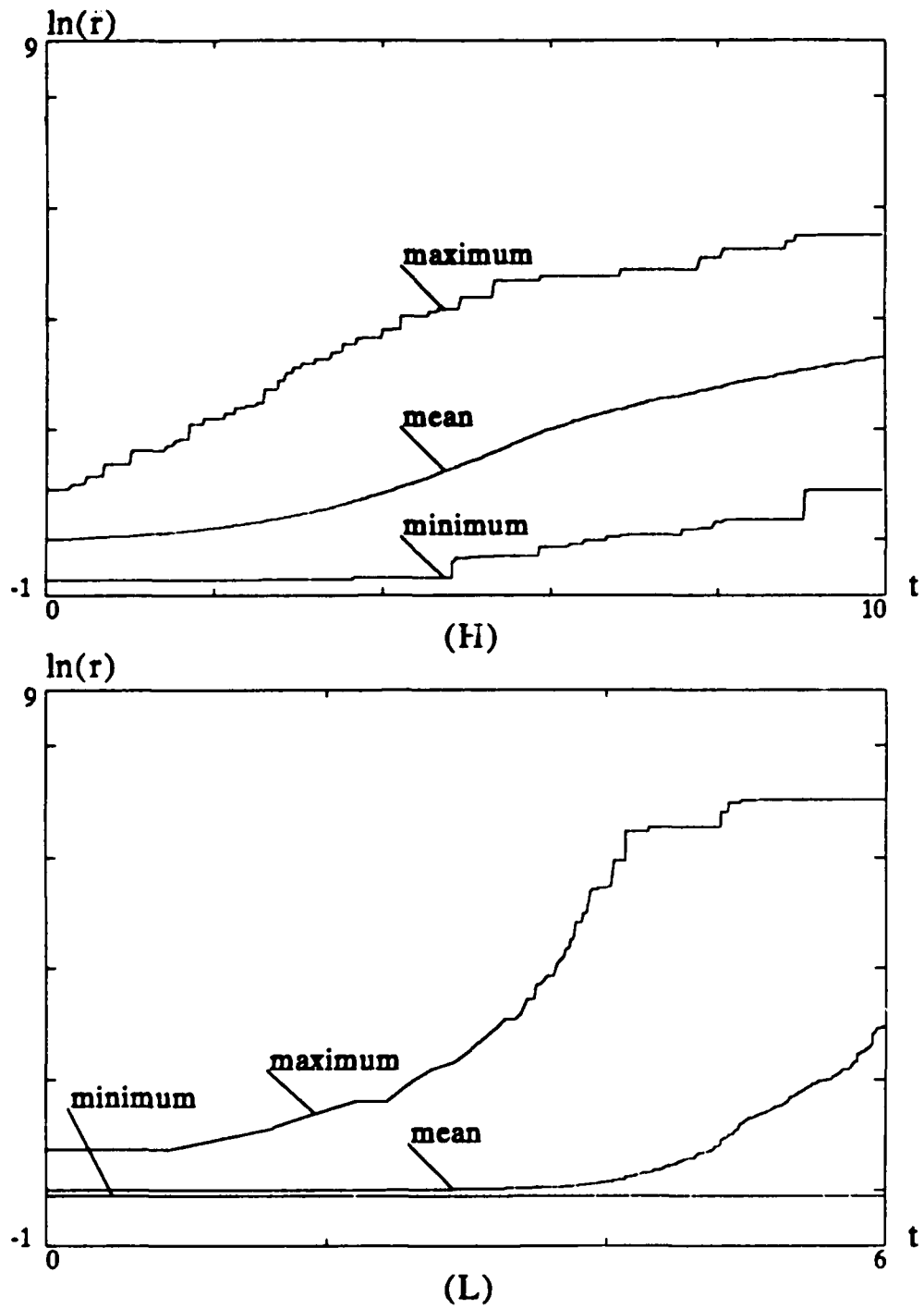


Fig. 4.5 log of minimum, mean and maximum bubble radius vs. time. (H) corresponds to run H, and (L) corresponds to run L.

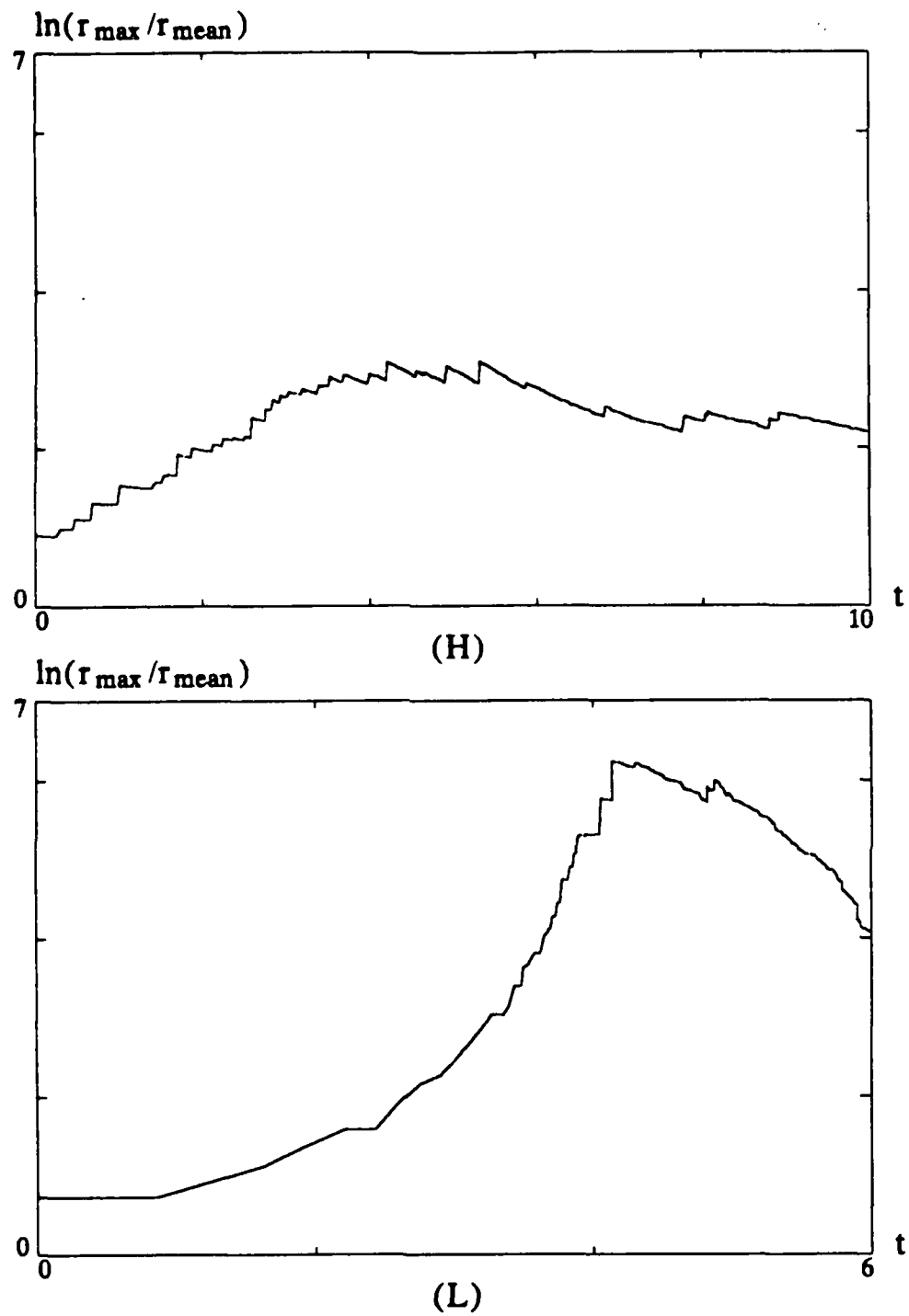


Fig. 4.6 $\ln(r_{\max}/r_{\text{mean}})$ vs. time. (H) corresponds to run H, and (L) corresponds to run L.

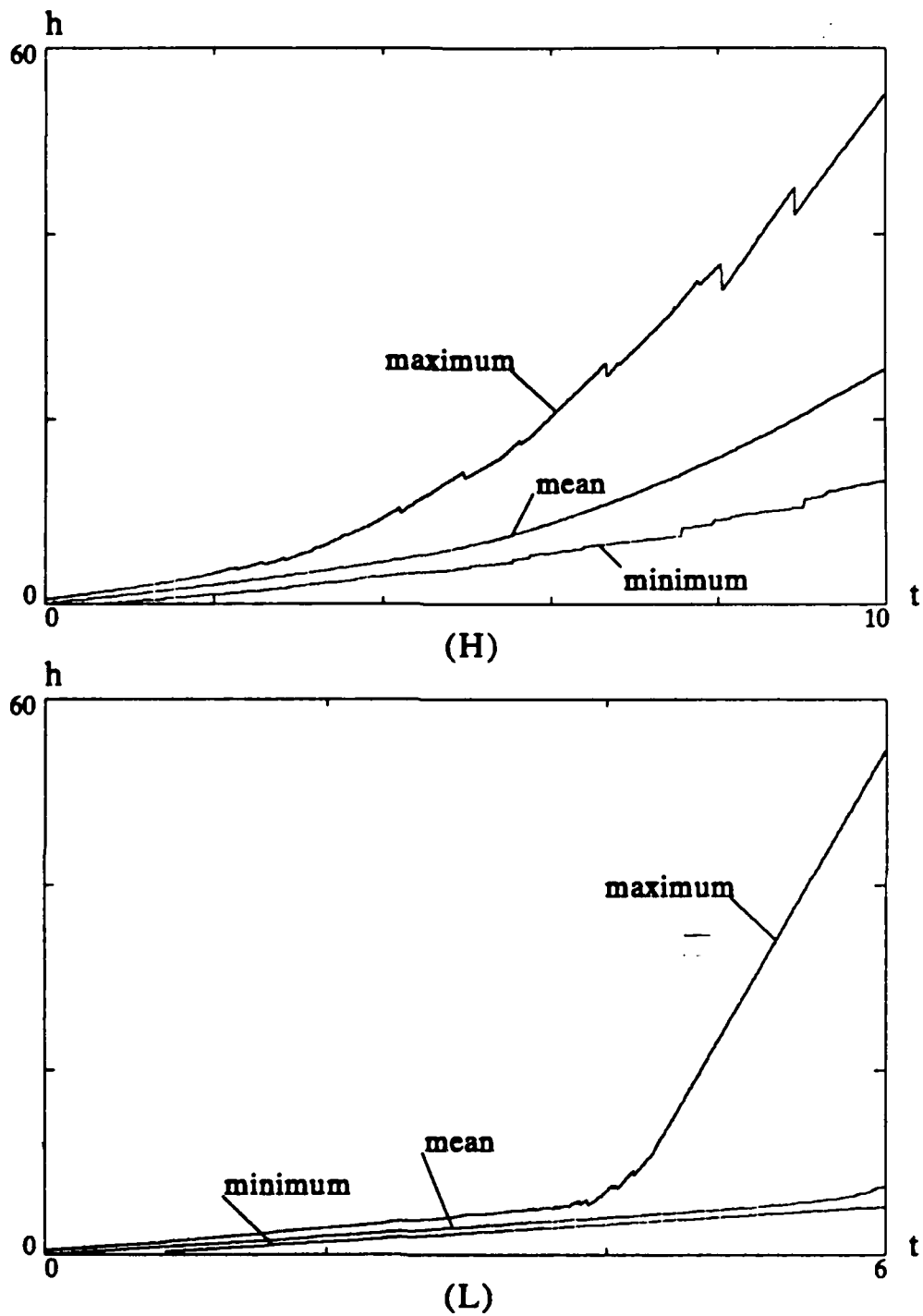


Fig. 4.7 minimum, mean and maximum bubble height vs. time. (H) corresponds to run H, and (L) corresponds to run L.

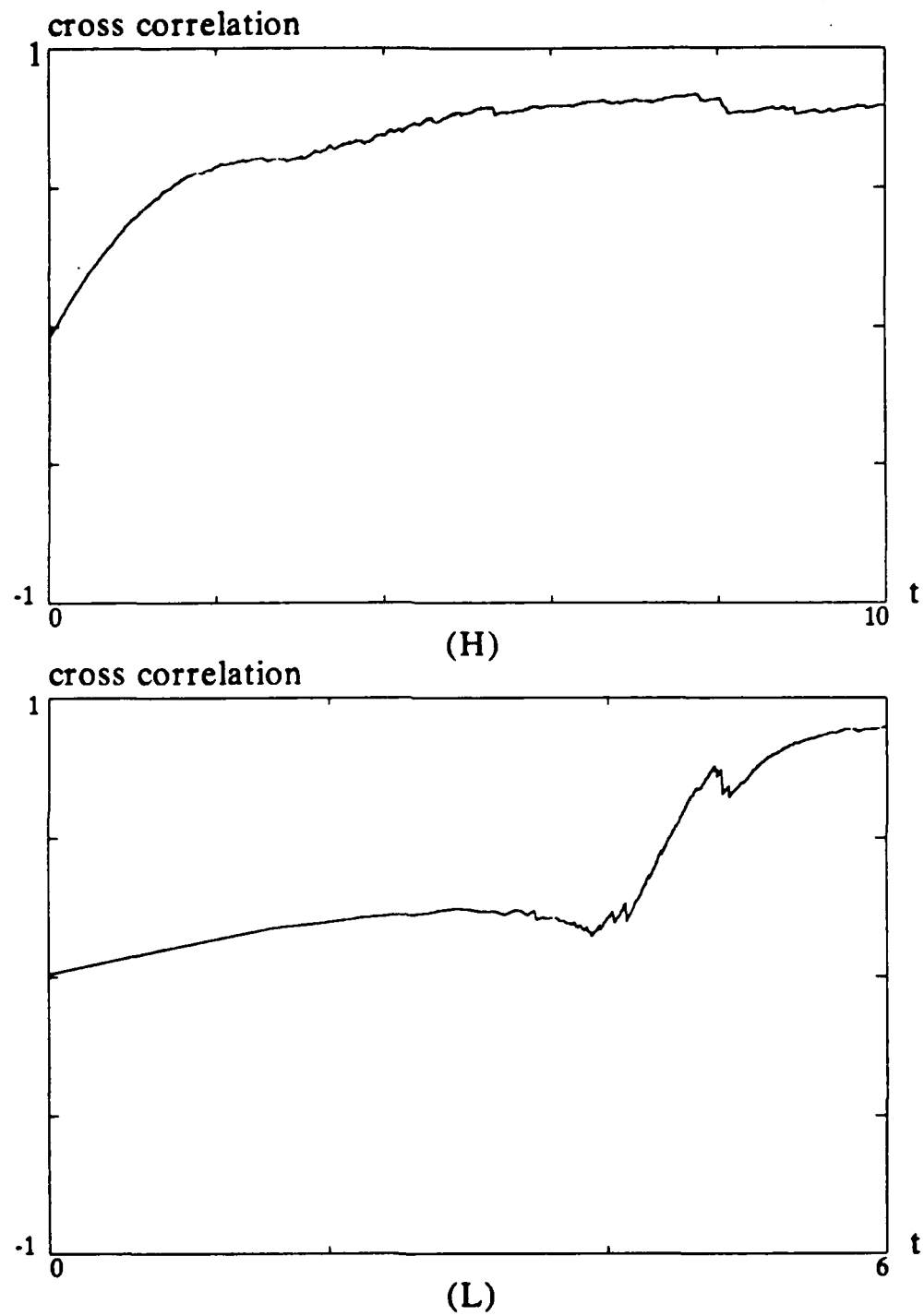


Fig. 4.8 radius, height cross correlation vs. time. (H) corresponds to run H, and (L) corresponds to run L.

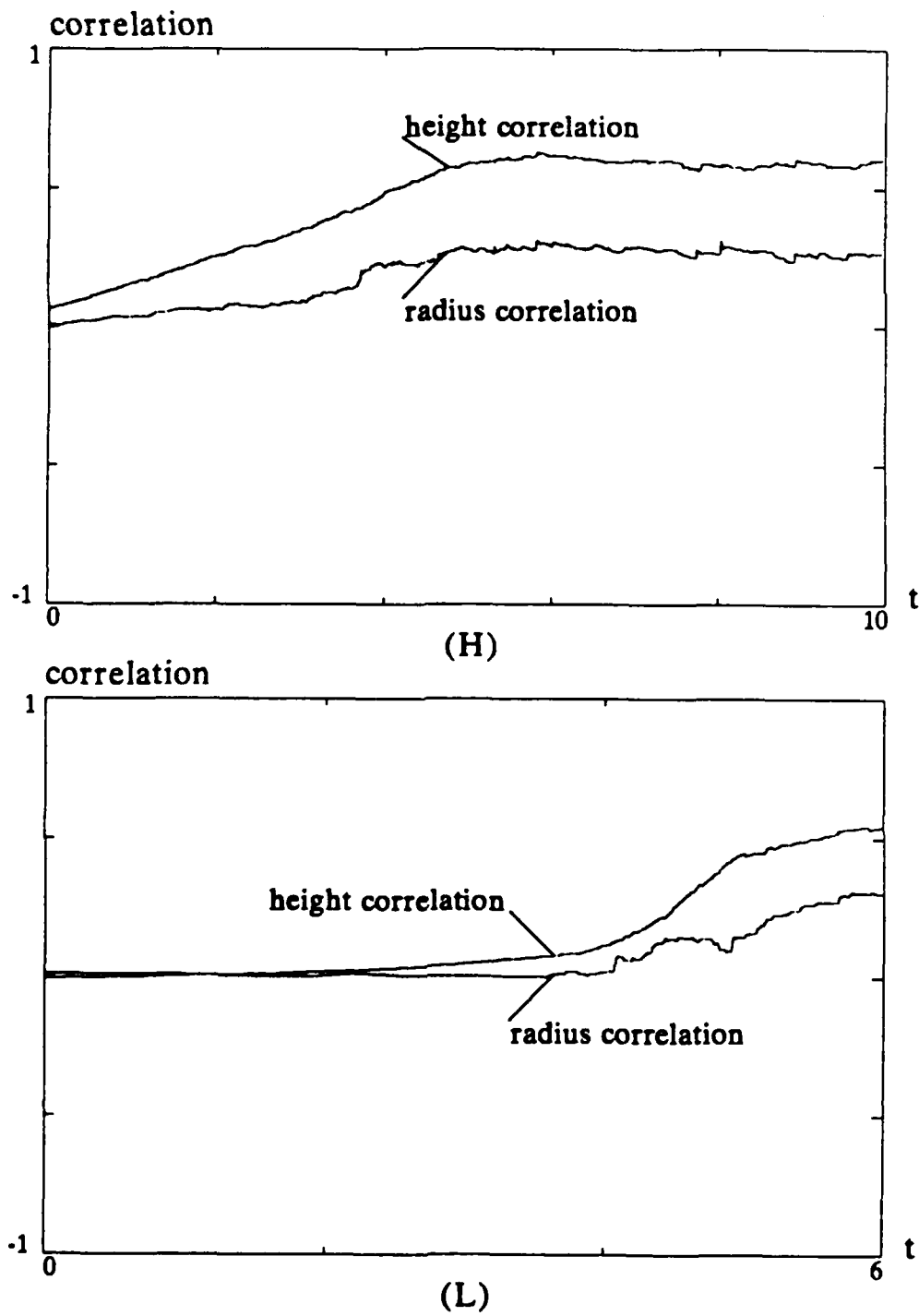


Fig. 4.9 radius and height correlation vs. time. (H) corresponds to run H, and (L) corresponds to run L.

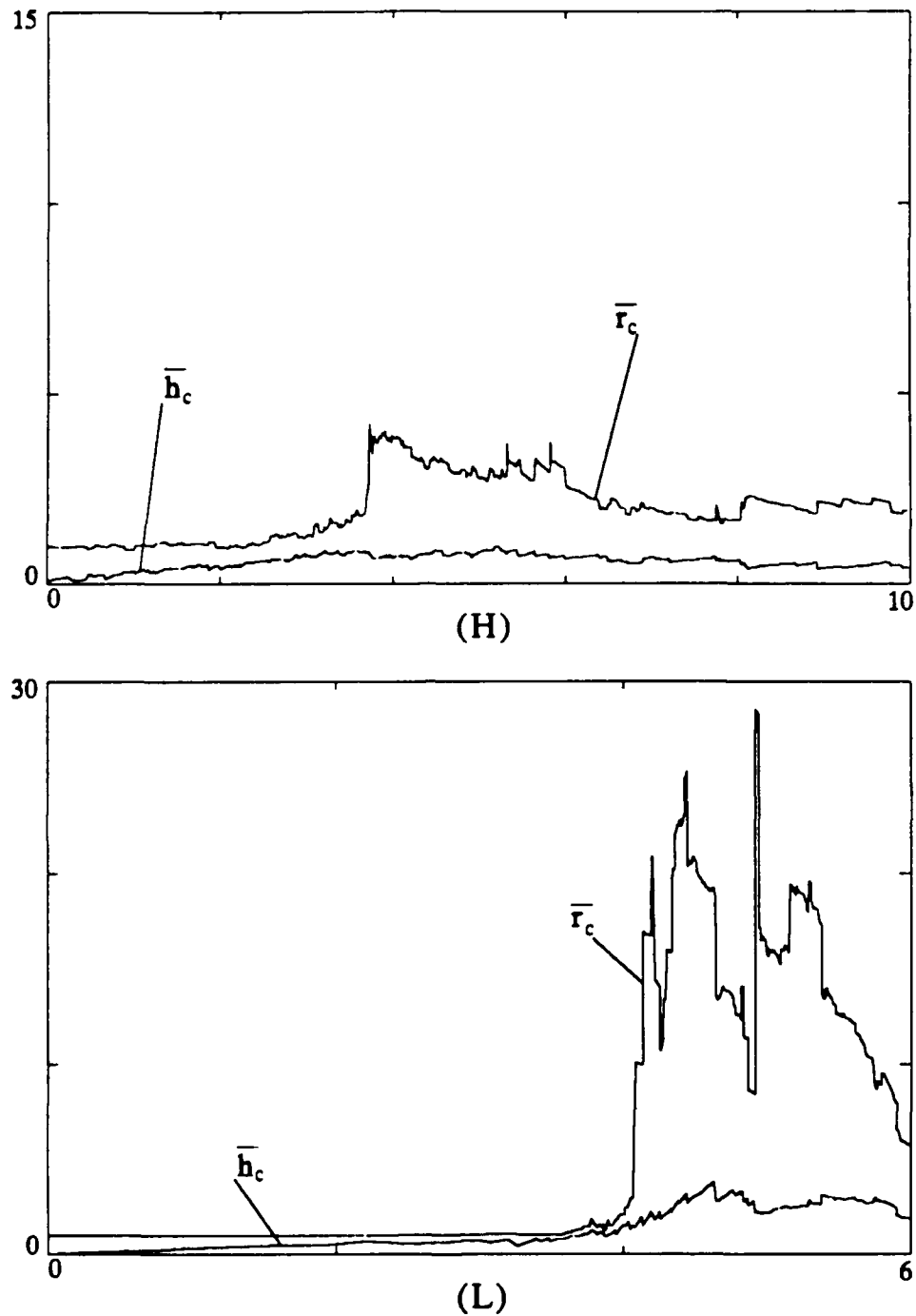


Fig. 4.10 The expected scaled radii \bar{r}_c and height \bar{h}_c of bubbles adjacent to large bubbles are plotted as a function of time. The y axis is in units of dimensionless length. This plot should be contrasted to Fig. 4.5 and Fig. 4.7, which display mean radius and height without restriction.

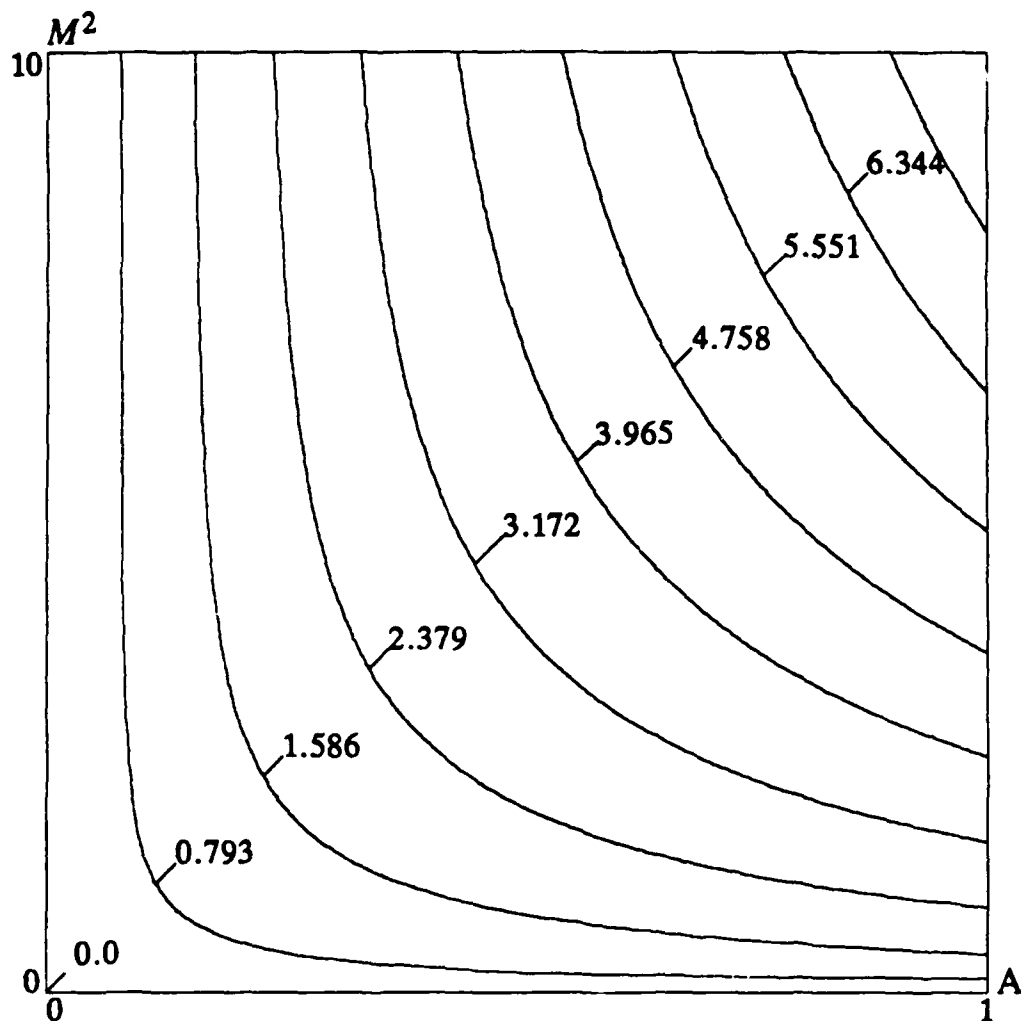
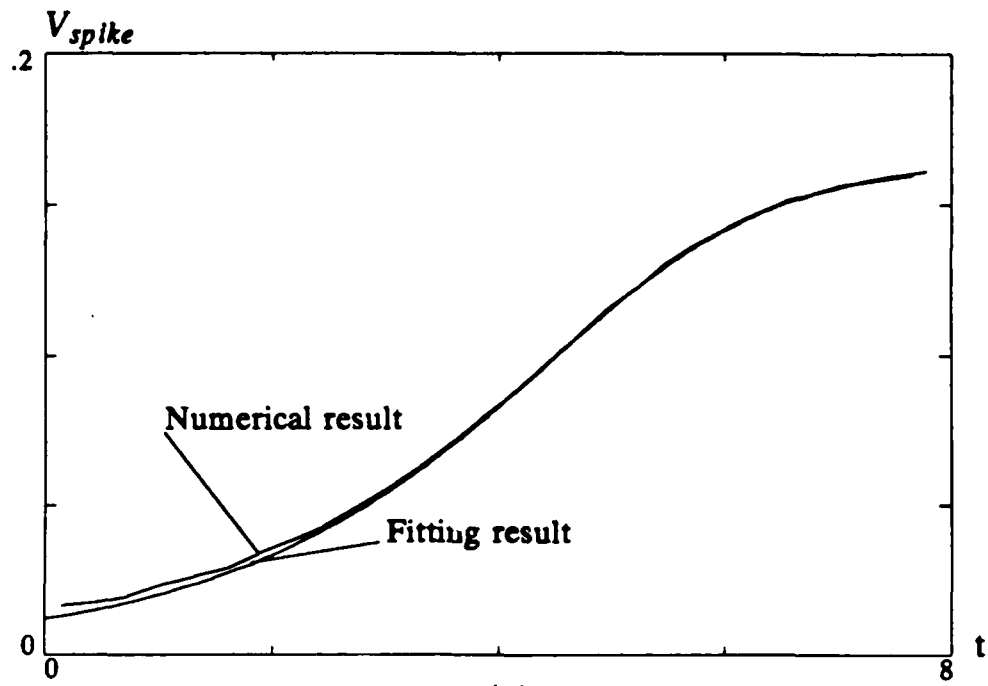
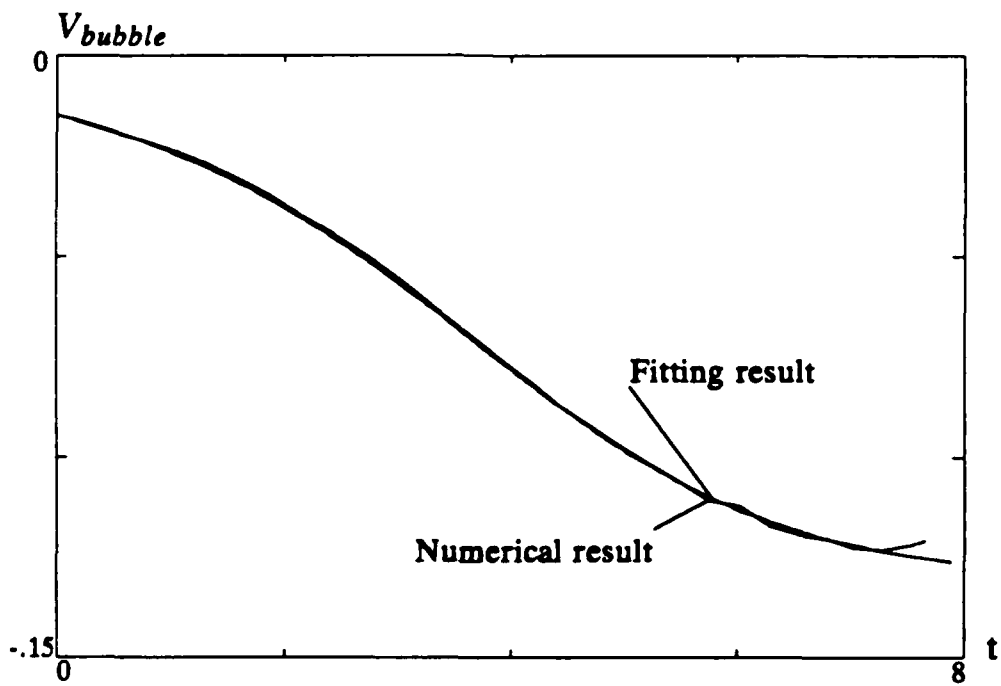


Fig. 5.1 The dependence of the dimensionless growth rate on A and M^2 . The difference between two adjacent constant contours is 0.793.



(a)



(b)

Fig. 5.2 Plots of spike velocity and bubble velocity versus time are shown with the best two parameter fit to equation (21) superimposed, for the parameter values $D = 2$, $M^2 = 0.5$, $\gamma = 1.4$. The numerical results are obtained by using a 80 by 640 grid in a computational domain 1×8 .

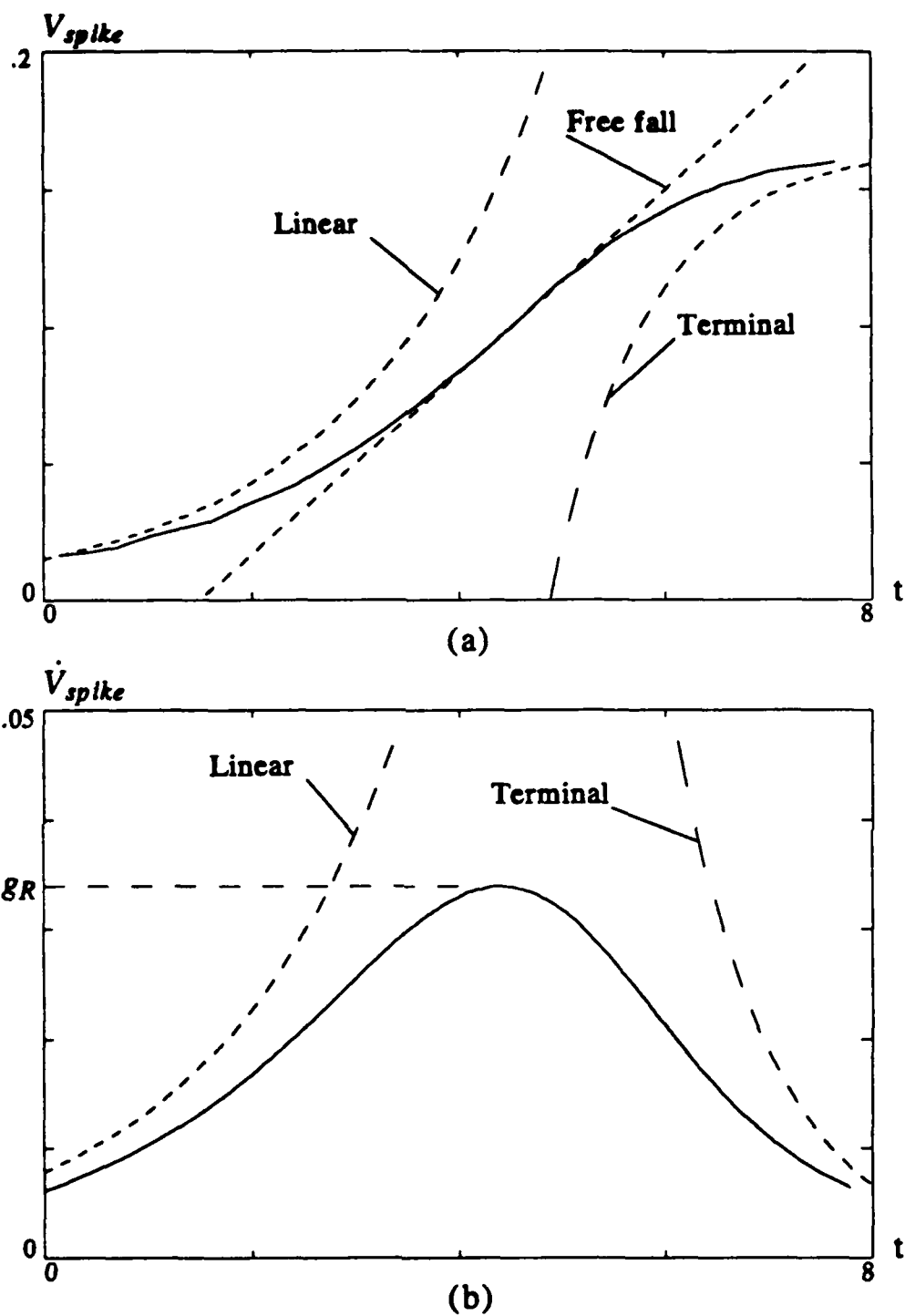


Fig. 5.3 The comparison of the spike velocity and the spike acceleration of the numerical result to its linear and large time asymptotic behavior for $D = 2$, $M^2 = .5$ and $\gamma = 1.4$. The solid lines are the numerical results obtained by using a 80 by 640 grid in a computational domain 1×8 .

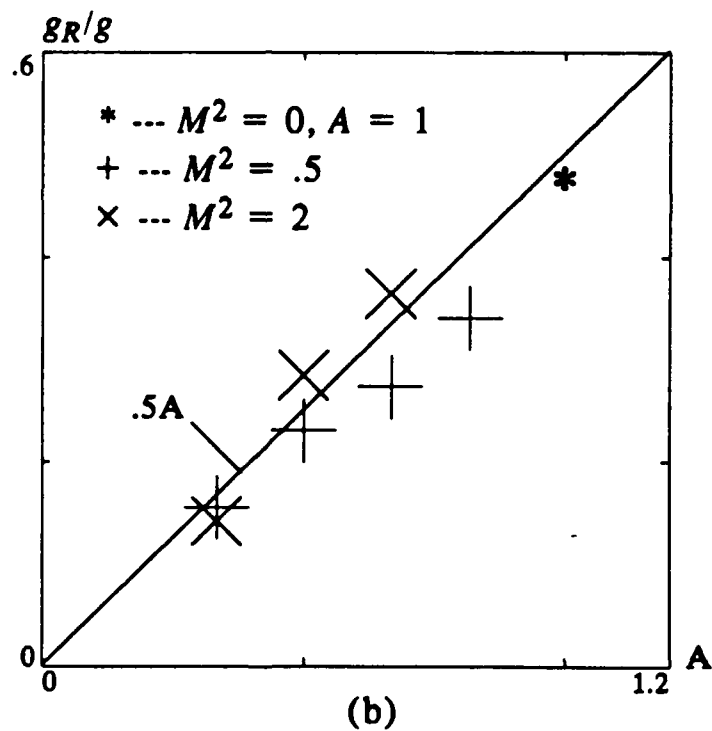
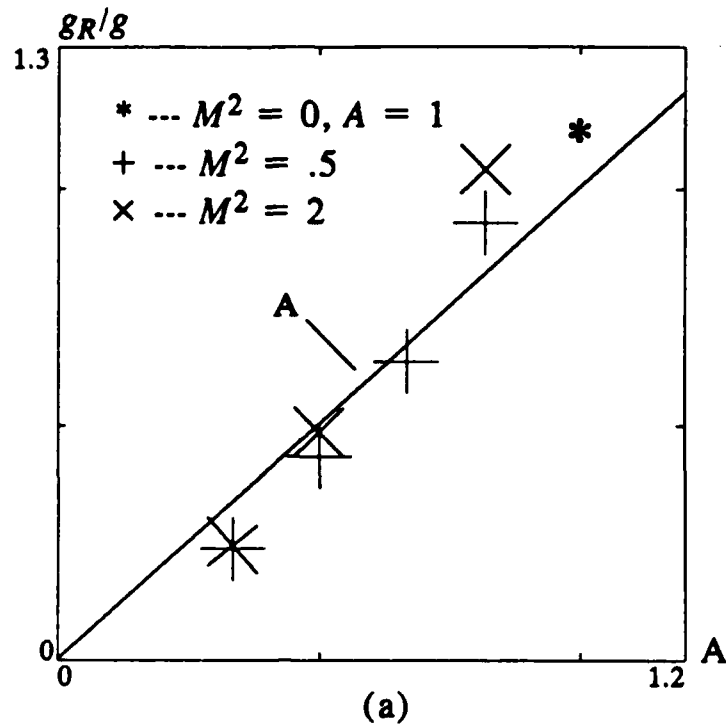


Fig. 5.4 The plots of the renormalization factor for gravity versus the Atwood ratio for (a) spike and (b) bubble. For comparison, the straight lines which are proportional to the Atwood ratio are also plotted. The data for a one component, incompressible fluid ($A = 1, M^2 = 0$) is taken from reference 20.

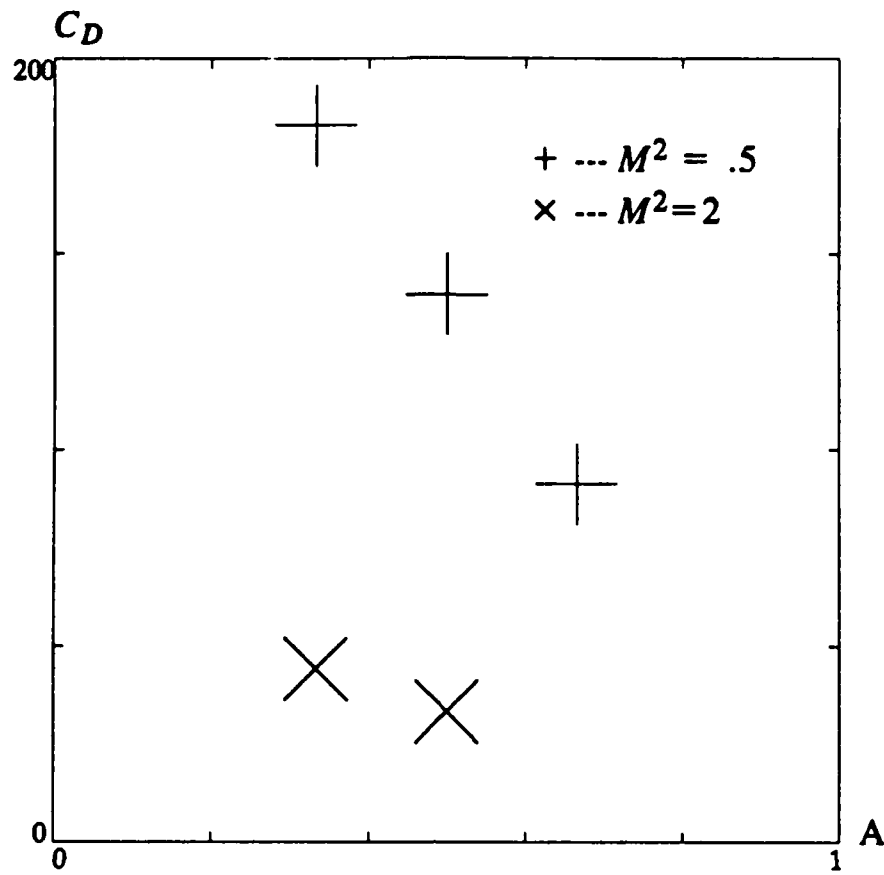
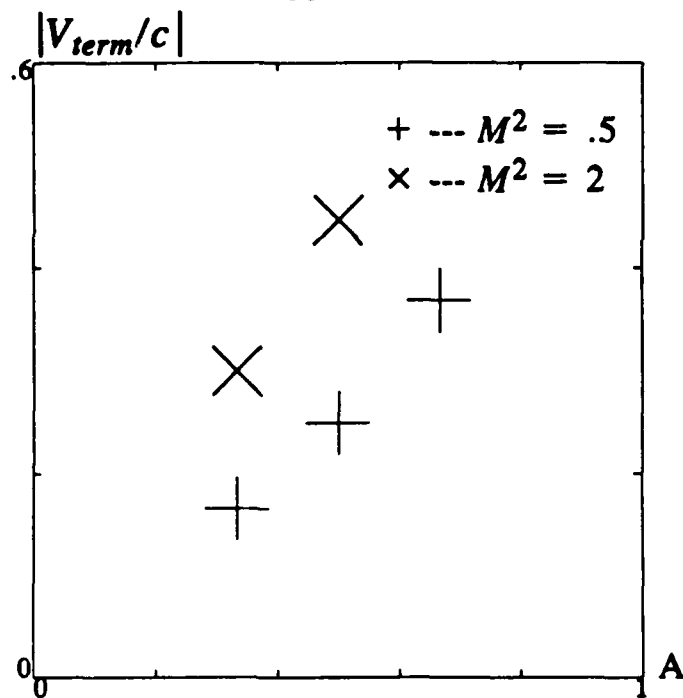
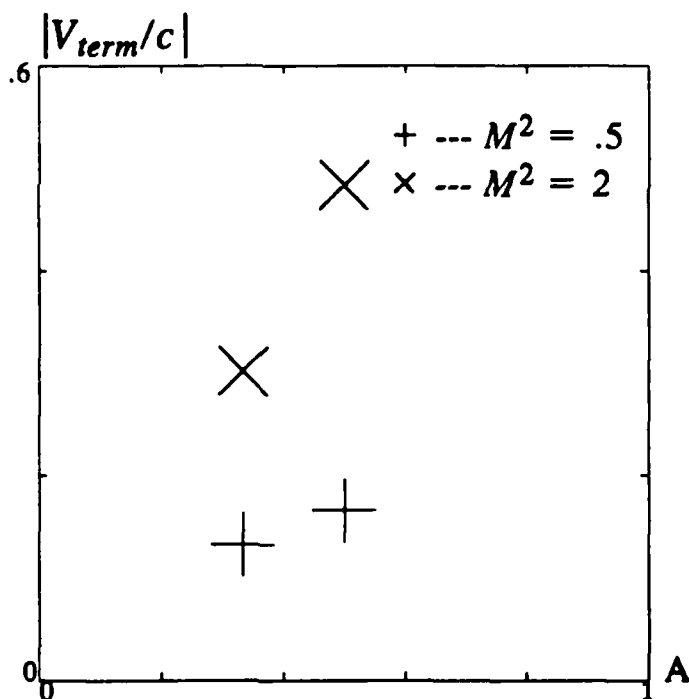


Fig. 5.5 The plot of the spike drag coefficient C_D versus the Atwood ratio for $M^2 = .5$ (+) and 2 (x) and $\gamma = 1.4$. Note that for $A = 1$, $C_D = 0$ on theoretical grounds and this suggests an empirical relation $C_D = \text{const} (1 - A)$ with the constant dependent on M .



(a)



(b)

Fig. 5.6 Plots of Mach number (the ratio of the terminal velocity to the sound speed of the heavy gas) of (a) spike and (b) bubble versus the Atwood ratio. The high density ratio systems have not reached the terminal velocity region at the end the computation. Therefore the terminal velocity can not be determined in these systems. The spike and the bubble velocities at the last computation step are supersonic (relative to the sound speed of the heavy gas) in the $D = 10$ and 100 cases. In the incompressible case ($M^2 = 0$), $|v_{term}/c| = 0$ by definition.

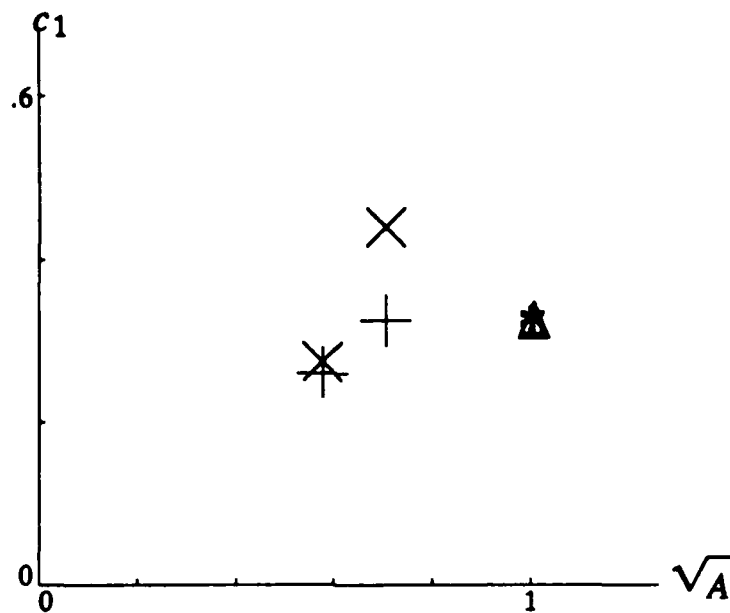


Fig. 5.7 A plot of the constant c_1 versus the square root of the Atwood ratio for $D = 2$ and 3, $M^2 = .5$ (+), 2 (x), and $\gamma = 1.4$. The values of c_1 calculated from the two (*) and Δ) dimensional incompressible ($M^2 = 0$, $A = 1$) theories are also shown. The value for (*) comes from reference 21 and Δ) comes from reference 22.

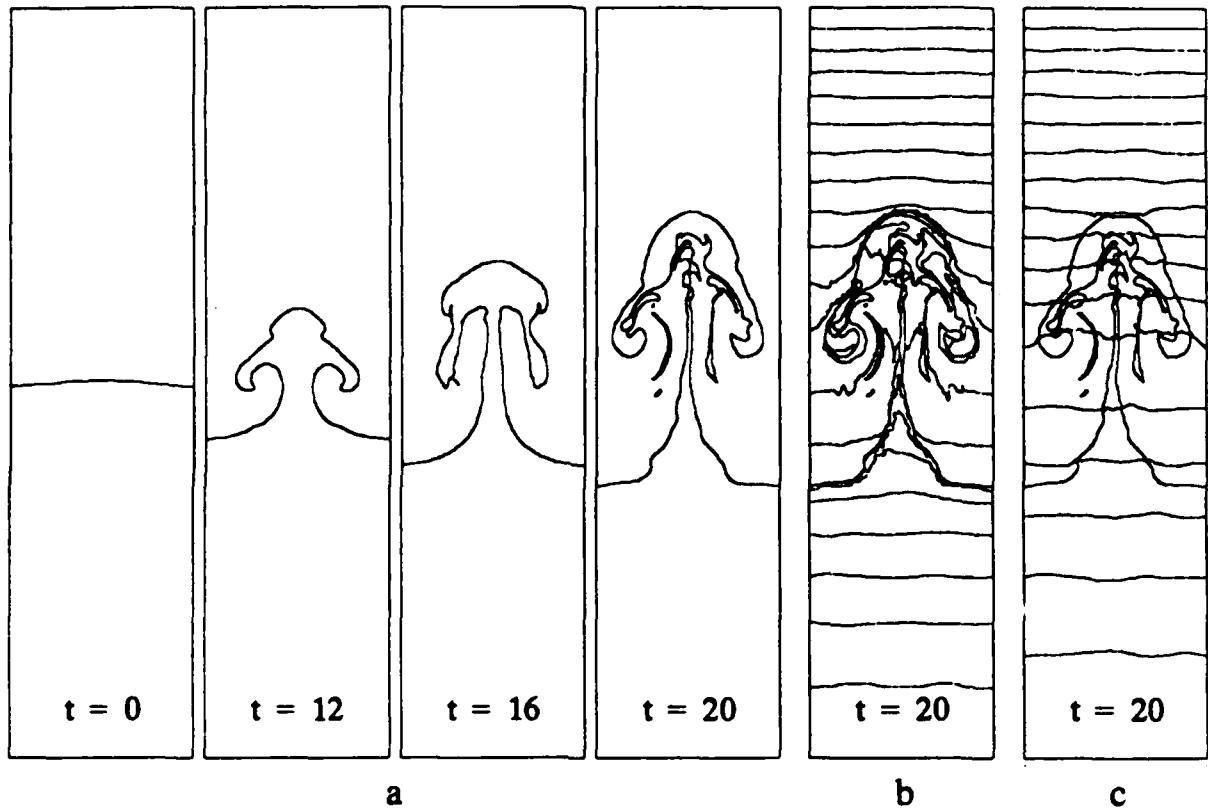


Fig. 5.8 Plots of the interface position, density and pressure contours for $D = 1.5$, $M^2 = .5$, $a = .015$, $\gamma = 1.4$ in a computation domain 1×6 with a 40 by 240 grid. Only the upper two thirds of the computational region is shown in the plot because nothing of interest occurs in the remainder of the computation. (a) The interface position for successive time steps. (b) The density contour plot. (c) The pressure contour plot.

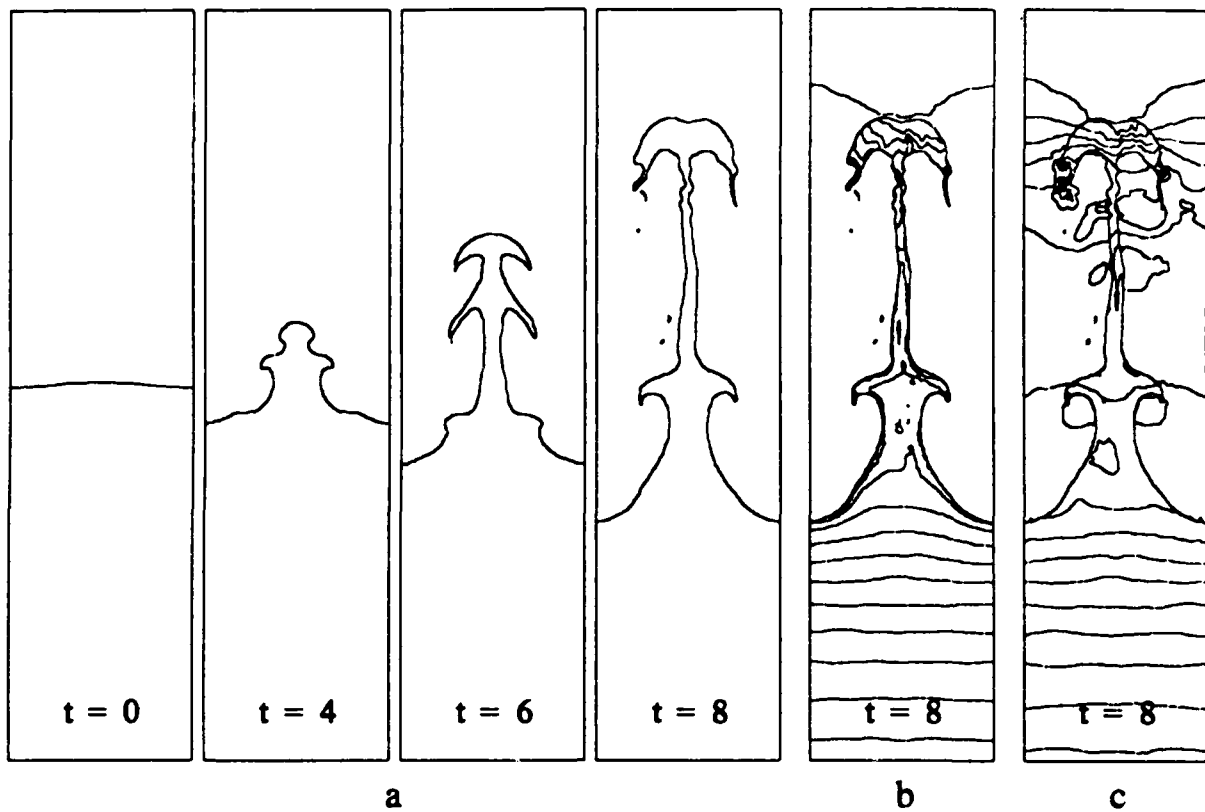


Fig. 5.9 Plots of the interface position, density and pressure contours for $D = 10$, $M^2 = .5$, $a = .015$, $\gamma = 1.4$ in a computation domain 1×4 with a 40 by 160 grid. (a) The interface position for successive time steps. (b) The density contour plot. (c) The pressure contour plot.

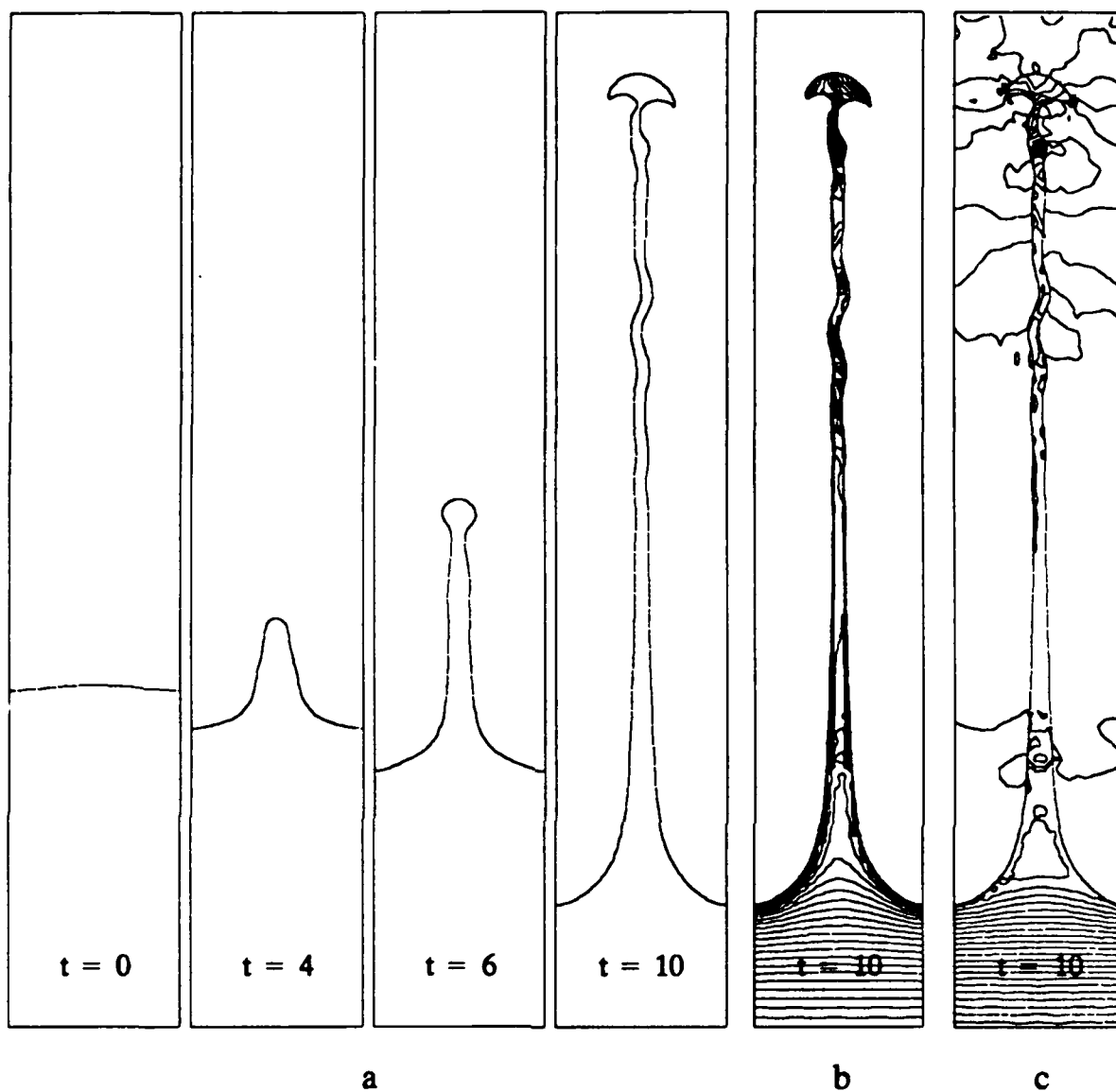
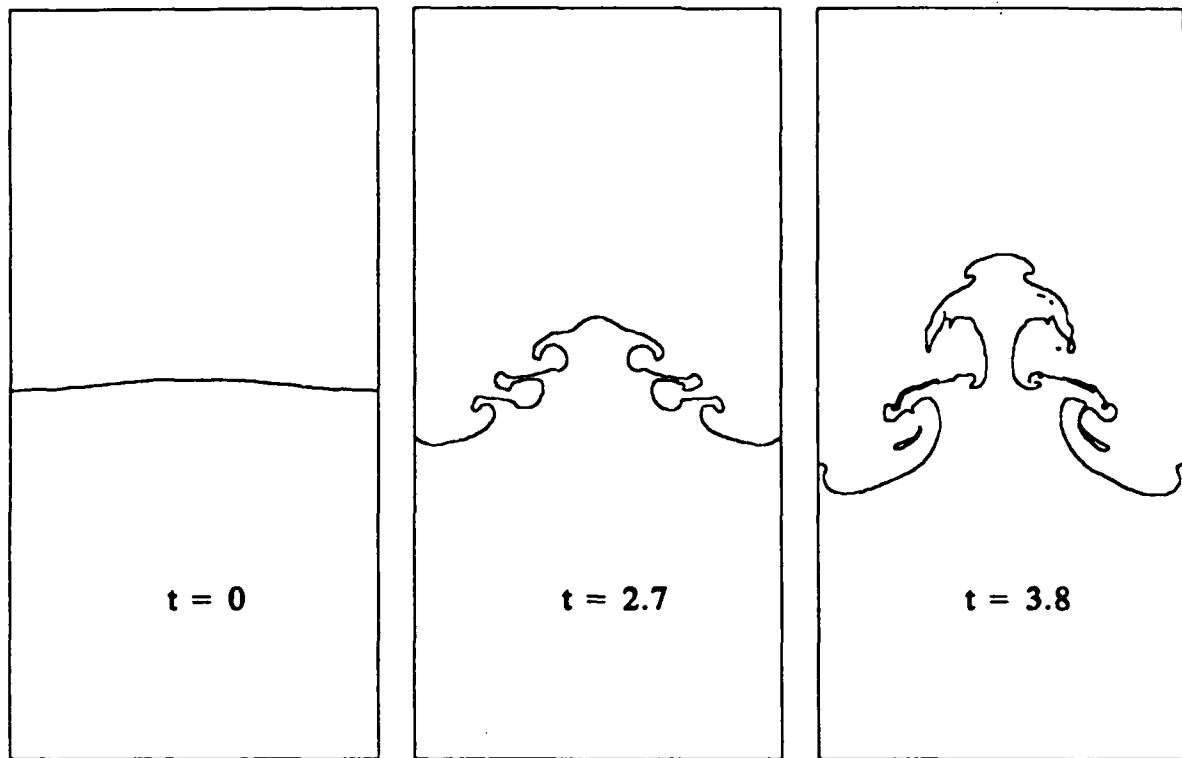


Fig. 5.10 Plots of the interface position, density and pressure contours for $D = 100$, $M^2 = .5$, $a = .015$, $\gamma = 1.4$ in a computation domain 1×10 with a 20 by 200 grid. Only the upper four fifths of the computational region is shown in the plot because nothing of interest occurs in the remainder of the computation. (a) The interface position for successive time steps. (b) The density contour plot. (c) The pressure contour plot.



a

Fig. 5.11 Plots of the interface position for success time steps for $D = 2$, $M^2 = 2$, $A = .015$, $\gamma = 1.4$ in a computation domain 1×8 with 80 by 640 grids. Only the middle part the computational region is shown because nothing of interest occurs in the remainder of the computation.

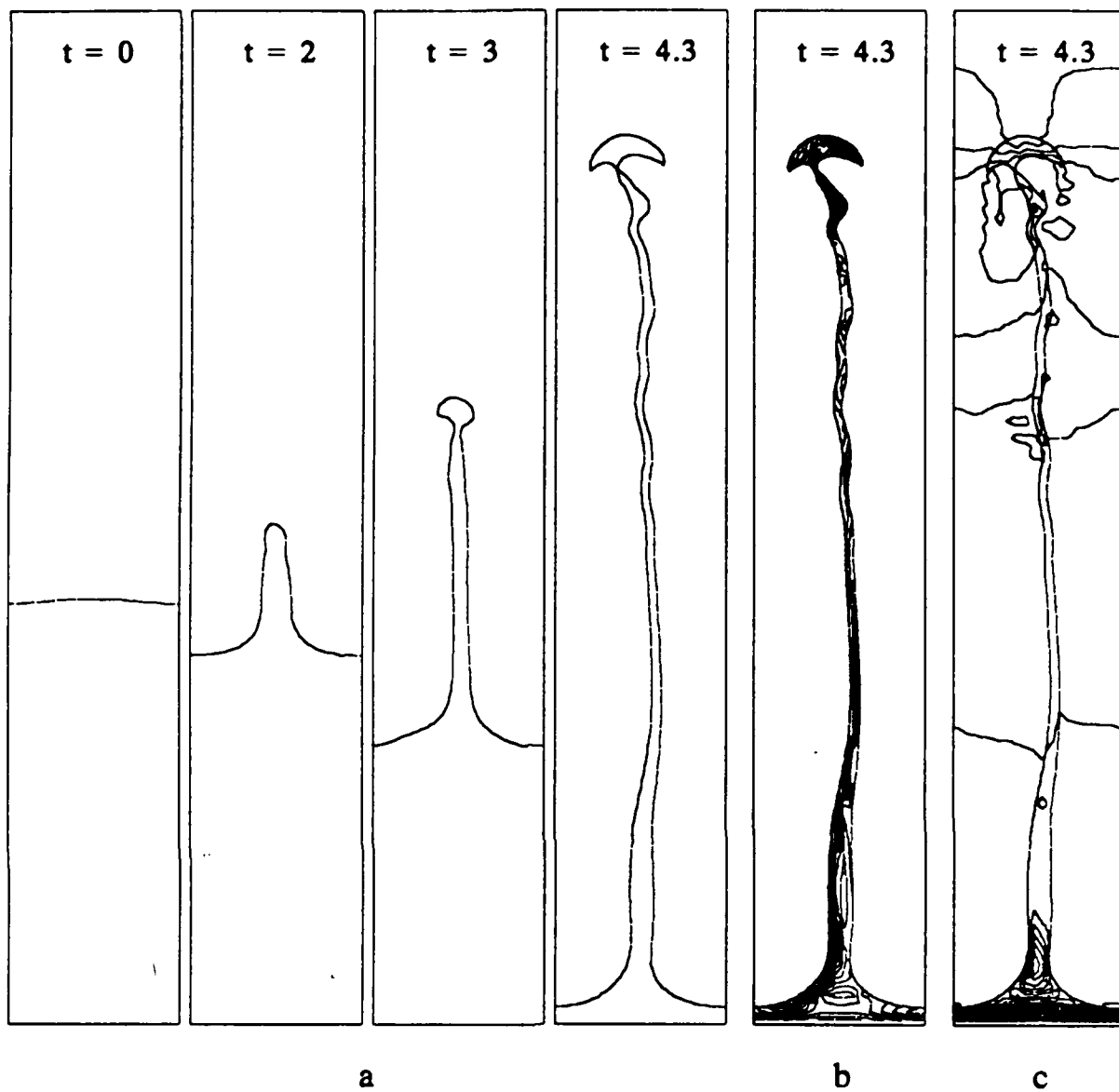


Fig. 5.12 Plots of the interface position, density and pressure contours for $D = 100$, $M^2 = 2$, $a = .015$, $\gamma = 1.4$ in a computation domain 1×6 with a 20 by 120 grid. (a) The interface position for successive time steps. (b) The density contour plot. (c) The pressure contour plot.

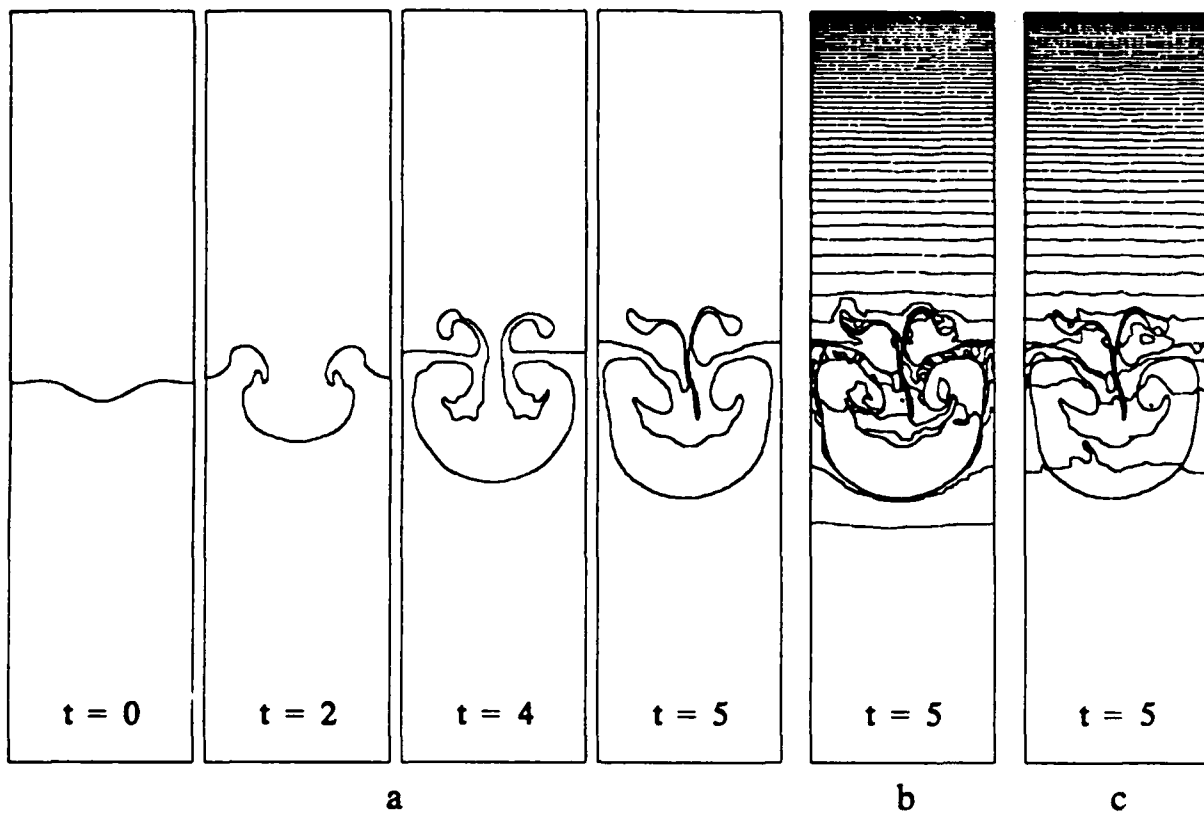


Fig. 5.13 Plots of the interface position, density and pressure contours of a bubble merger for $D = 2$, $M^2 = 2$, $\gamma = 1.4$ in a computation domain 1×4 with a 75 by 300 grid. (a) The interface position for successive time steps. (b) The density contour plot. (c) The pressure contour plot.

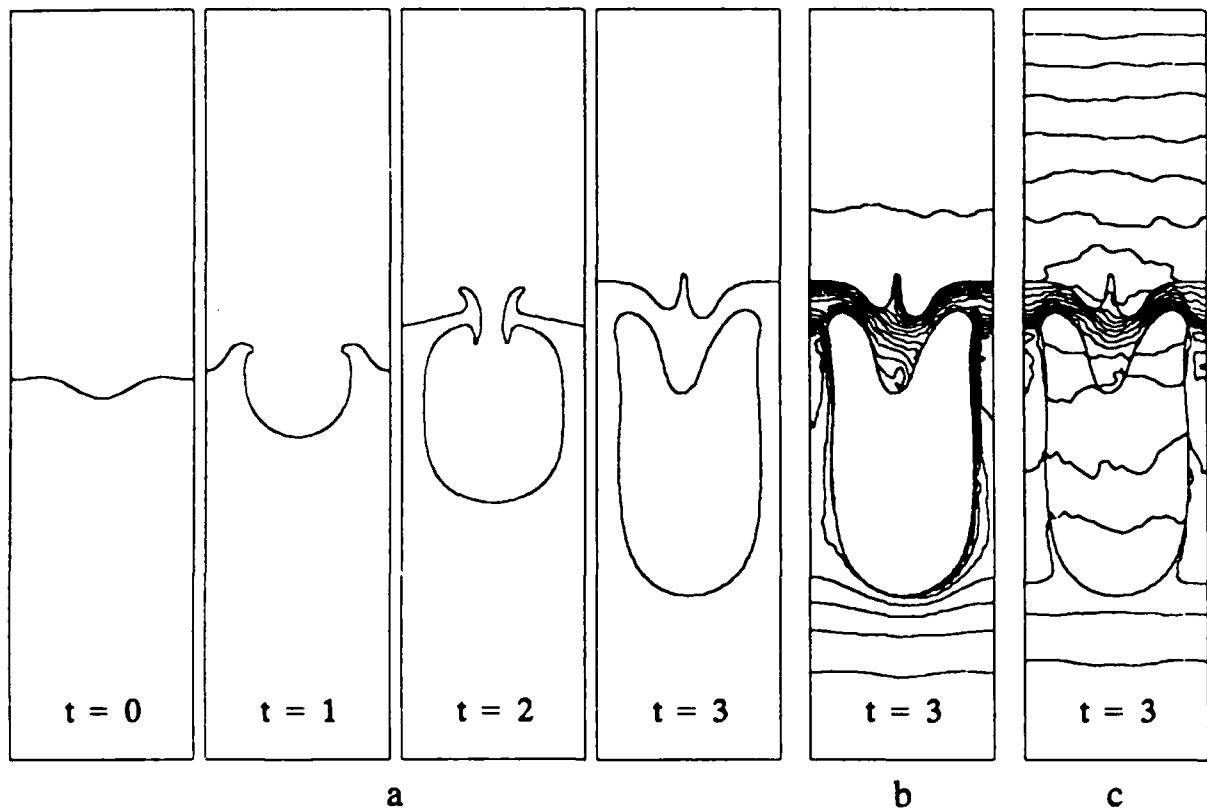
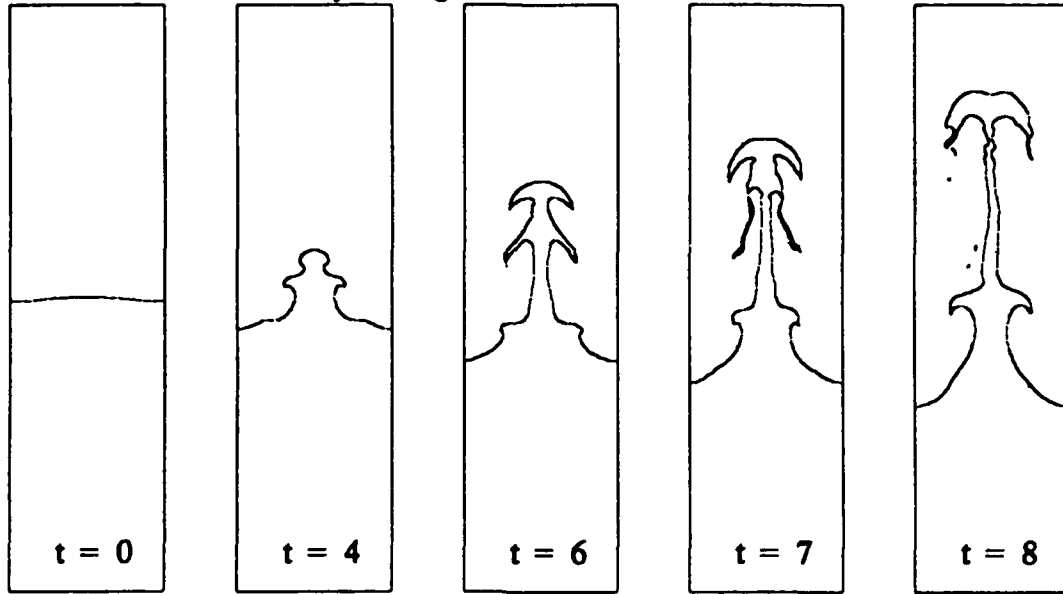


Fig. 5.14 Plots of the interface position, density and pressure contours of a bubble merger for $D = 10$, $M^2 = 2$, $\gamma = 1.4$ in a computation domain 1×4 with a 75 by 300 grid. (a) The interface position for successive time steps. (b) The density contour plot. (c) The pressure contour plot.

The fronts for 40 by 160 grids:



The fronts for 10 by 40 grids:

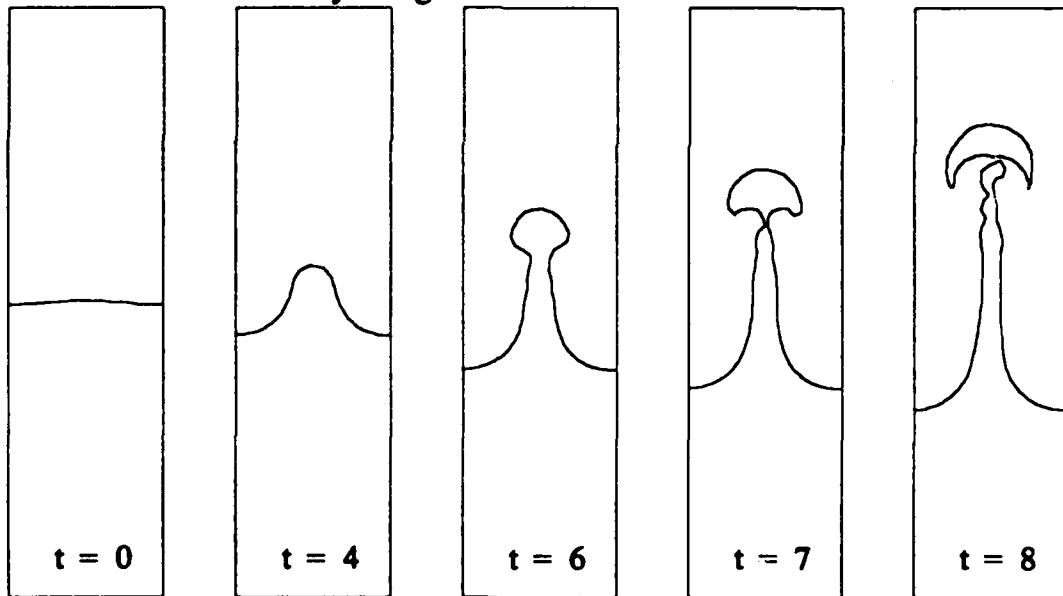


Fig. 6.1 Positions of the front at a sequence of time steps for $D = 10$, $M^2 = 0.5$ and $a = 0.015$ by using 40 by 160 and 10 by 40 grids. The finer grids resolve the more detailed structure of the interface.

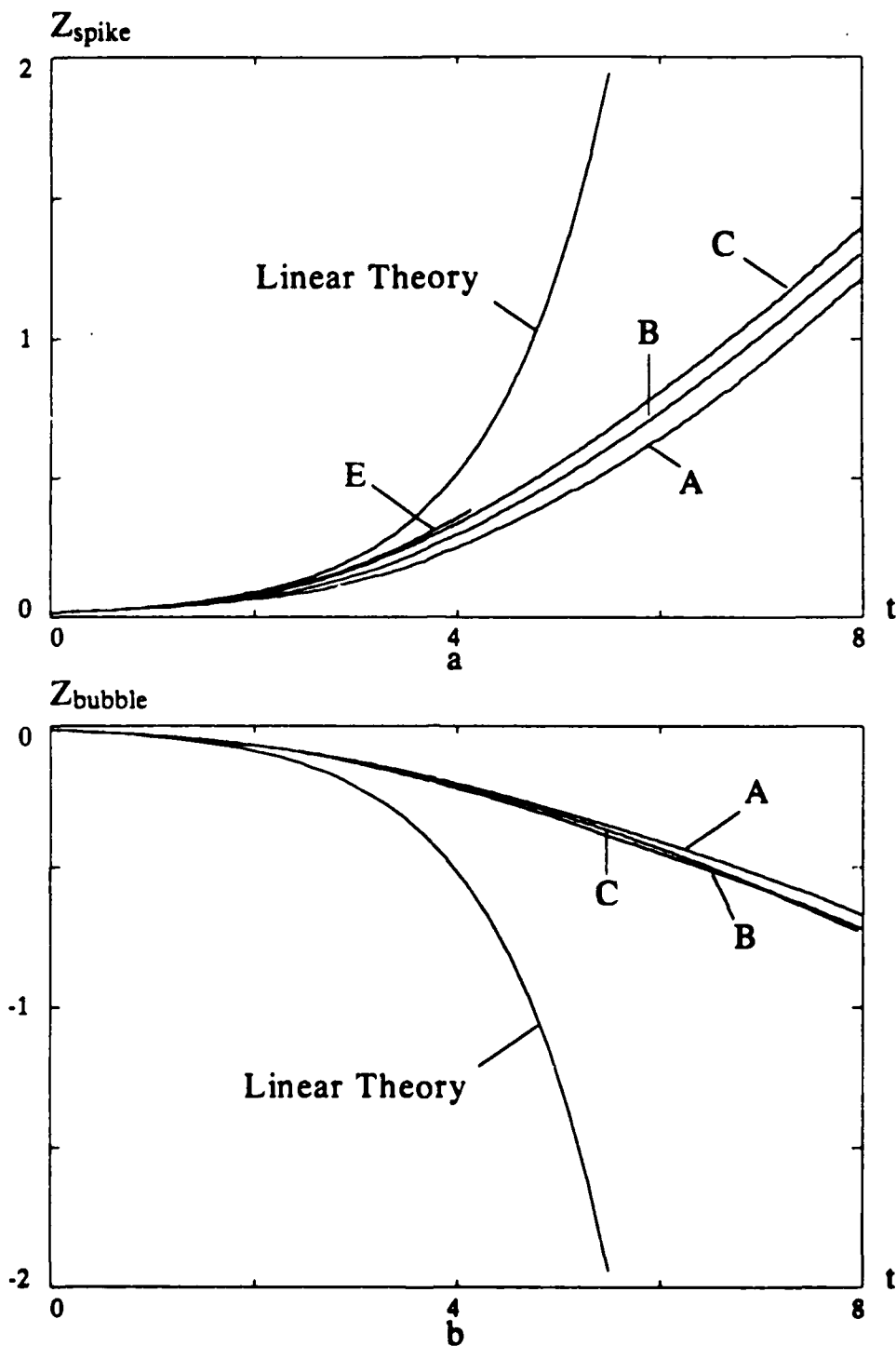


Fig. 6.2 A comparison of the position of the spike and the bubble for $D = 10$, $M^2 = 0.5$ and $a = 0.015$ using (A) 10 by 40, (B) 20 by 80, (C) 40 by 160 and (E) 80 by 320 grids. Plot a is the position of the spike. Plot b is the position of the bubble. For comparison, the linear theory is also shown. As can be seen, most of the computation is out of the linear regime.

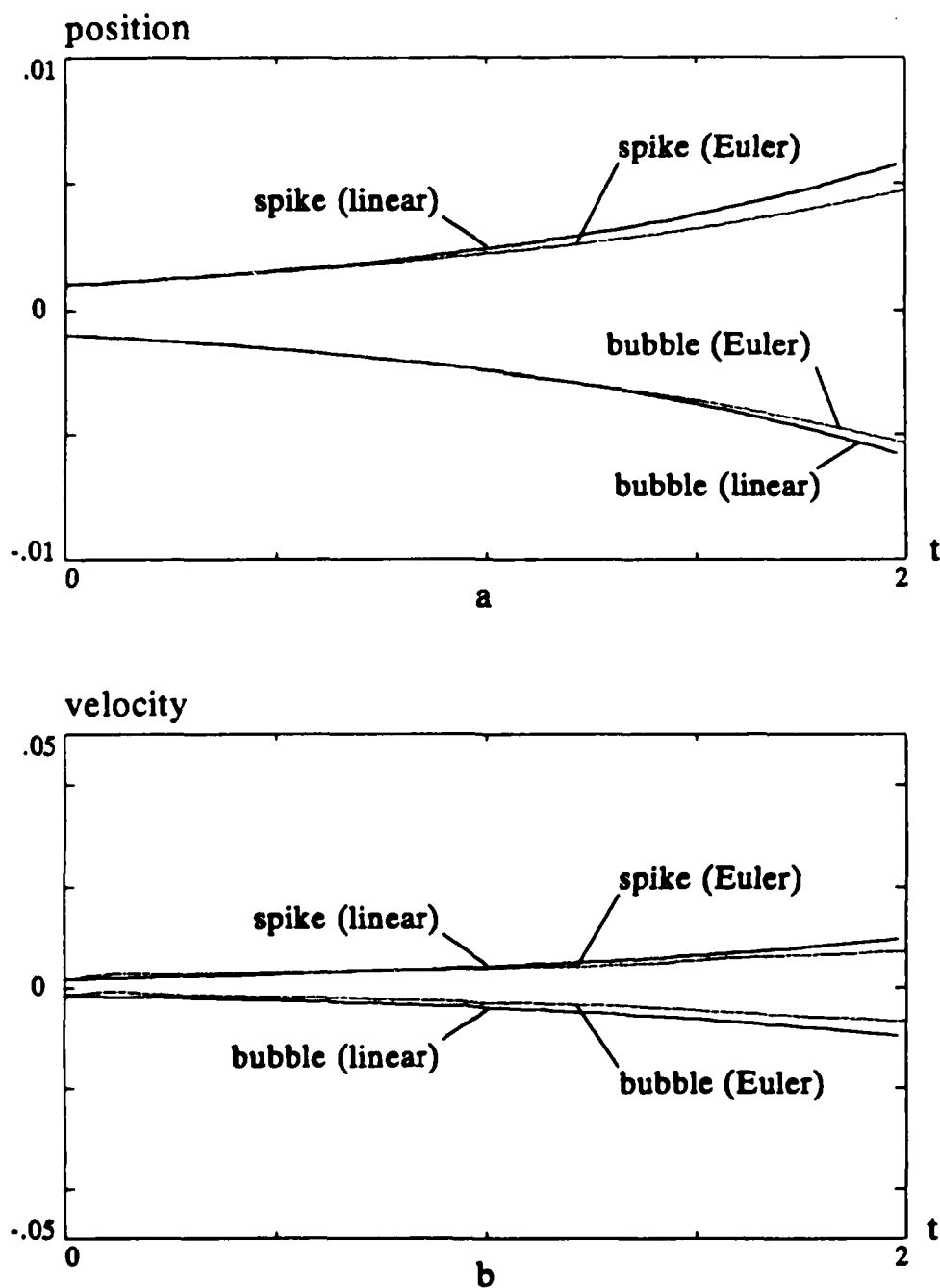


Fig. 6.3 A comparison of the spike and the bubble velocity and position for the linear theory and the full Euler equations. Here $D = 10$, $M^2 = 0.5$ and $a = 0.001$. A 40 by 160 grid was used in a computational region of size 1 by 4.

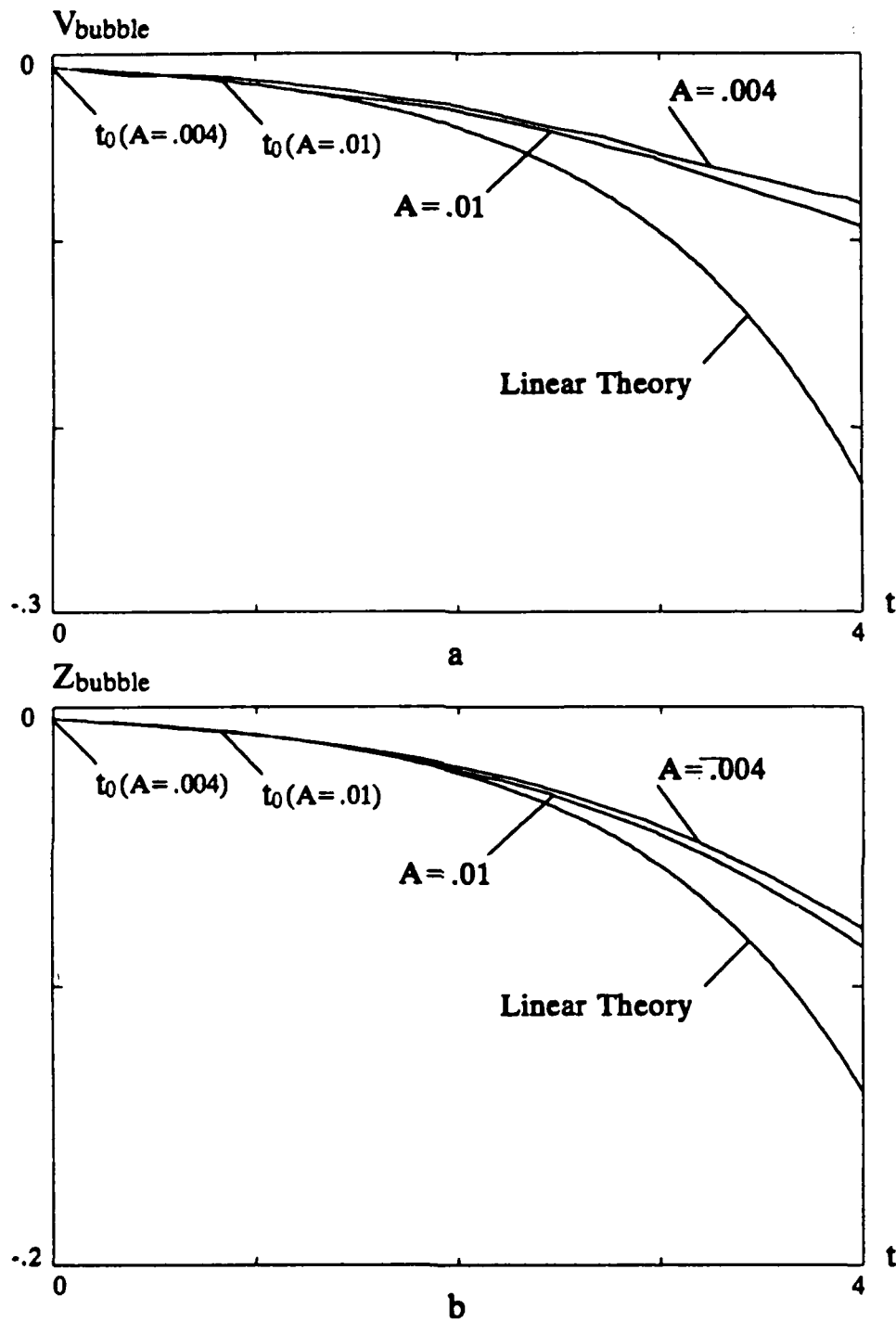


Fig. 6.4 A comparison of different initial starting amplitudes for $D = 10$, $M^2 = 0.5$, $a = 0.004$ and $A = 0.01$ using a 40 by 320 grid in a computational region of size 1 by 4. The time plot is terminated at $t = 4$ because for $a = 0.004$, the one way reflected waves in the heavy gas arrive at the interface shortly after that and the agreement between these two runs does not and should not persist after this time.

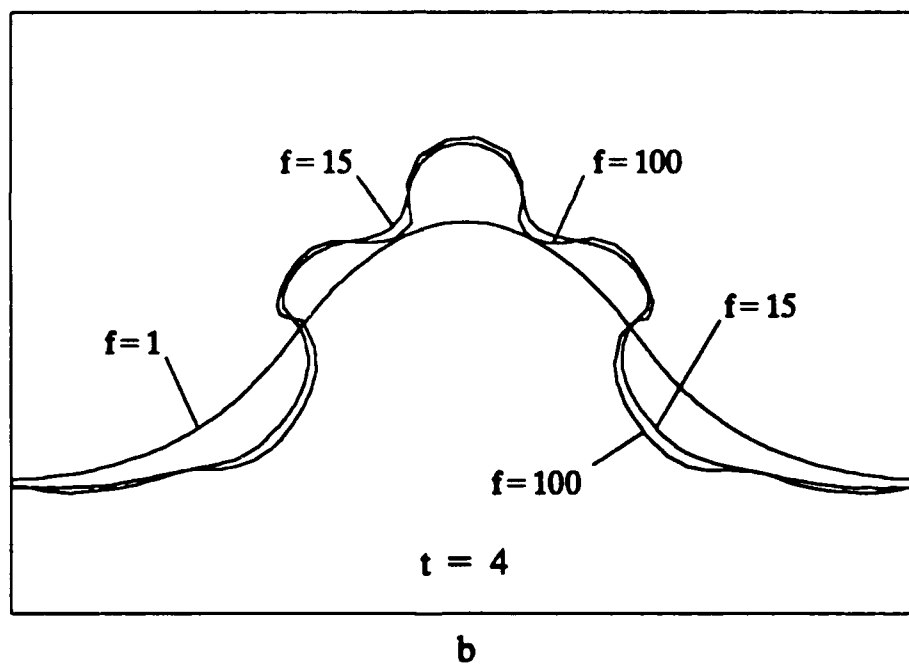
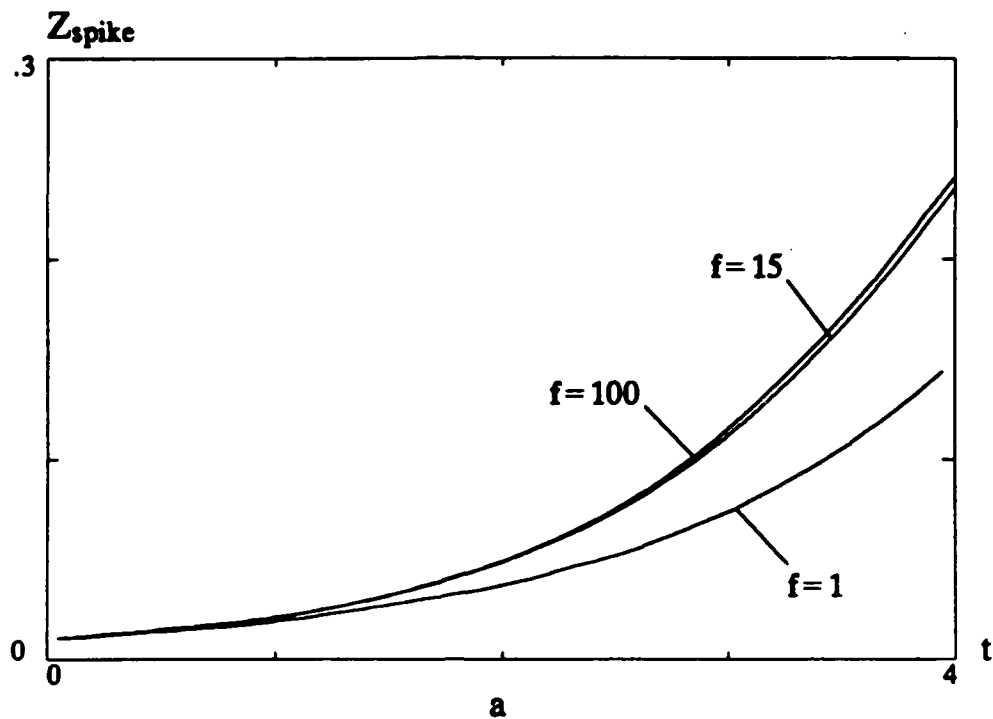


Fig. 6.5 A comparison of different redistribution frequencies for $D = 10$, $M^2 = 0.5$ and $a = 0.01$ with a 40 by 160 grid in a computational region of size 1 by 4. $f = 1, 15, 100$ corresponds to redistributing the front every 1, 15, 100 time steps. Plot *a* is for the position of the spike. Plot *b* is for the interface. Compare to frame 2 of Fig. 6.1.

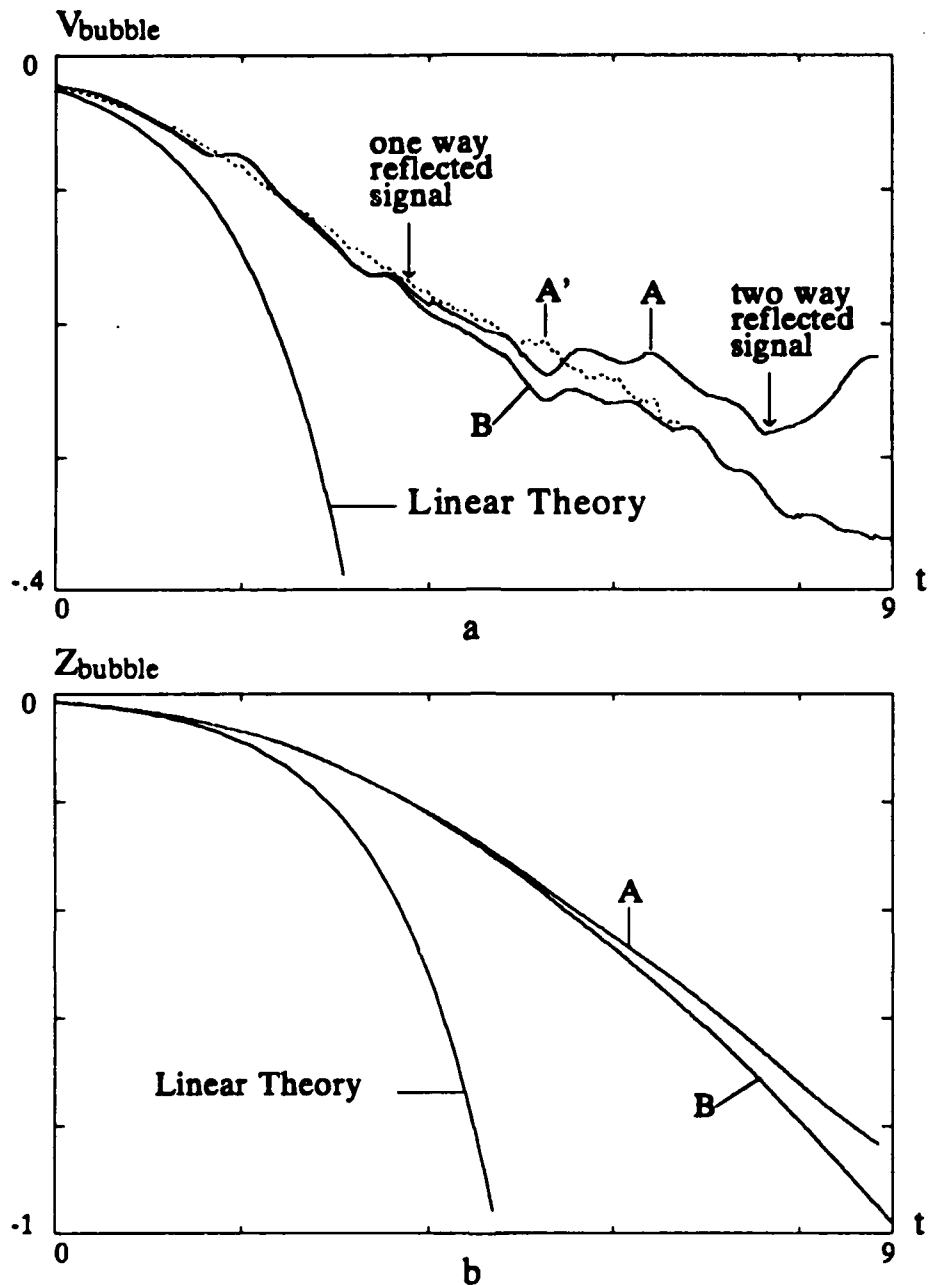


Fig. 6.6 A comparison of boundary effects for a domain of shape 1×4 (A) and 1×8 (B) with 10 by 40 and 10 by 80 grids respectively. Here $D = 10$, $M^2 = 0.5$ and $a = 0.015$. The one way reflected wave corresponds to a signal from the nearest boundary. The two way reflected wave corresponds to a signal starting from the interface. Plot a is for the velocity of the bubble. Plot b is for the position of the bubble. For distinguishing the boundary effects from the grid effects, a 40 by 160 grid curve (A') in the computation domain 1×4 is also plotted as a dotted line in the plot a . The wiggles which are common to A and B (and missing in A') are grid effects, while the divergence between A and B, marked by the arrival of the one way and two way reflected signals are pure boundary effects.

END

10-87

DTIC